Rank-based predictive control for community microgrids with dynamic topology and multiple points of common coupling

by

Brevann Nun

B.S., Kansas State University, 2019

A THESIS

submitted in partial fulfillment of the requirements for the degree

MASTER OF SCIENCE

Mike Wiegers Department of Electrical and Computer Engineering
Carl R. Ice College of Engineering

KANSAS STATE UNIVERSITY
Manhattan, Kansas

2021

Approved by:	Approved by:
Co-Major Professor	Co-Major Professor
Dr. Hongyu Wu	Dr. Mohammad B. Shadmand

Copyright

Abstract

The devastating effects of climate change paired with increasing geopolitical tensions and rising energy needs have prompted the development and incorporation of renewable energy technologies with the bulk power system in recent decades. Rapid advancements in technologies such as solar photovoltaics (PV) and wind harvesting devices have led to the proliferation of distributed energy resources at the distribution level. Decreasing costs of renewable energy systems and the ever-present dangers of climate change facilitate an increase in the saturation of these resources at the grid edge. However, a high penetration of intermittent energy generation dependent on solar irradiance and wind speed, as well as limited storage availability, creates challenges of grid resiliency and stability. A potential solution to overcome the aforementioned operational challenges is to realize hierarchical grid clusters with flexible boundaries towards resilient operation of future power grids. These hierarchical grid clusters, forming the entire grid, are also known as a grid of microgrids or grid of nanogrids. Hierarchical clusters of distributed energy resources (DERs) forming a grid of microgrids can share power more efficiently. A microgrid can operate in grid-connected or islanded modes which provide resiliency by supplying local loads within the microgrid boundary during natural disasters or other anomalies in power grid. The flexible boundaries of these microgrids requires multiple points of common coupling (MPCC) with adjacent microgrids and the rest of the power network which makes their synchronization challenging. Thus, in a power grid comprising a network of microgrids and MPCC, control and synchronization of voltage source converters (VSCs) is paramount to ensure optimal performance without jeopardizing network stability.

This thesis presents a rank-based model predictive controller (MPC) for VSCs operating in a community microgrid with dynamically changing topology representing the flexible

boundary of the microgrid. The proposed framework enables a fully synchronized microgrid with the ability to connect multiple distributed VSC buses to a utility grid simultaneously through MPCC. In addition, the control scheme offers redundancy to grid-forming sources when islanded, attaining a higher margin of resiliency, robustness, and flexibility. The MPC framework features an adaptive ranking system that assigns operational modes to the VSCs, i.e. voltage control (grid-forming) or current control (grid-following), and defines leader-follower directionality for synchronization. Communication among VSCs is achieved using a topology-mirroring communication layer. The presented framework enables transformative microgrid topologies based on the adaptive operation of distributed VSC controllers towards resilient power grids with high penetration of renewables.

Table of Contents

List of Figures

List of Tables

Acknowledgements

I would like to thank my friends, family, and wife for their unwavering encouragement and support. I would also like to express my sincere gratitude to Dr. Mohammad B. Shadmand and Dr. Hongyu Wu for their patience, wisdom, and guidance as they mentored me throughout my graduate academic career. Their support enabled me to successfully complete this thesis. Further, I would like to extend my thanks and appreciation to all members of the IPEG research group at the University of Illinois at Chicago whose continual encouragement and generous assistance helped me tremendously. Finally, I would like to thank the Kansas State University's Mike Wiegers Electrical and Computer Engineering department for providing me with the technical knowledge, lab infrastructure, and gracious support whenever required.

Chapter 1 - Introduction to Microgrids and MPCC

1.1 Motivation

The unregulated carbon-based emissions from fossil fuel power plants and automobiles throughout the twentieth century have had catastrophic consequences on Earth's climate [3]. The combustion of fuels such as coal, oil, and natural gas have long been known to release harmful pollutants into nearby ecosystems. Unprecedented levels of carbon dioxide and other greenhouse gases in the atmosphere cause a predictable and rapid rise in average global temperatures, resulting in elevated sea levels, ocean acidification, freshwater scarcity, and an increase in extreme weather phenomena [3-7]. Without immediate mitigation, these dangers are forecasted to continue and intensify well into the twenty-first century. In particular, major climate disasters are predicted to increase in frequency as they have in recent years [4]. Fig. 1.1 shows an alarming rise in major natural disaster events in the United States between 1980 and 2020, where each event constitutes a financial burden of more than one billion USD. This trend is relevant to

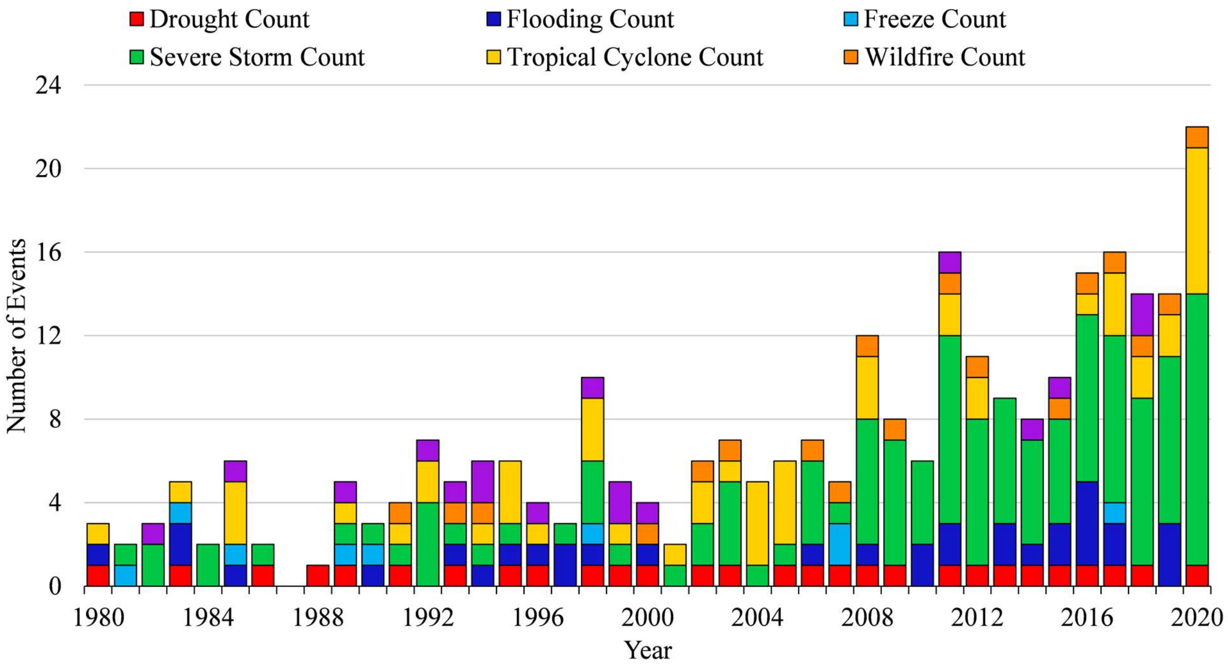

Fig. 1.1. 1980-2020 U.S. billion-dollar natural disaster event frequency.

the power sector both because the byproducts of traditional electric generation induce climate anomalies, and because these disasters threaten the physical infrastructure of the electric grid [8, 9]. For instance, the devastating winter storm of February 2021 left large sections of Texas without power for days or weeks while power-conserving blackouts rolled across much of the U.S. Midwest. As modern society relies more heavily upon consistent and robust electric power delivery, the physical vulnerabilities of the bulk power system present a greater risk of suspending power to critical loads. Solutions are needed to curtail the emission of greenhouse pollutants within the energy sector while improving the public power system's resiliency against natural and man-made hazards.

In response to environmental threats, rising energy demands, and as a means of mitigating a reliance on depleting foreign energy supplies, technologies to exploit sustainable energy resources have been developed in recent decades [10, 11]. Hydroelectric power has comprised the bulk of sustainable and renewable energy sources for decades, but its growth is now encountering the limits of physical terrain requirements [12]. In addition to a replenishing water source, such as a river, a hydroelectric dam demands expansive acreage to transform into a flooded reservoir. This reservoir presents its own environmental concerns and restricts proliferation. While still a major contributor of sustainable power, hydroelectric generation is not expected to observe a rapid rise in new capacity in the coming years. Nuclear power, once the assumed successor to fossil fuel generation, suffers from high costs, complex government bureaucracy, and potentially harmful byproducts. The development of new technologies for the deployment of nuclear resources is still a heavily researched topic, but atomic power is unlikely to become a widely adopted alternative to traditional generation in the near future.

In recent decades, a new generation of renewable energy technologies has emerged to supplant traditional fossil fuel generators [13]. Unlike their unrenewable counterparts, renewable energy systems such as solar photovoltaics (PV) and wind harvesting plants generate electrical energy from abundant, sustainable sources rather than through the combustion of fossil fuels. These power sources don't actively release pollutants into the environment as a byproduct of energy generation and typically require much less maintenance than their fossil-fueled counterparts. Penetration of renewable resources on the bulk utility grid has increased in recent years as the costs of such systems have declined while efficiency increased [14]. Surging energy needs and a corresponding rise in the cost of electrical power have made renewables financially competitive on the energy market. Simultaneously, the rise of distributed generation at the grid edge has led to the proliferation of localized solar and wind energy systems at the distribution level as consumers supplement their own power needs for financial or ecological gain. The projected 2020-2050 U.S. electrical generation capacity is depicted in Fig. 1.2, including a breakdown of renewable energy capacity by type [15]. As the demand for energy increases in the future, and as governments apply pressure to power sector leaders seeking environmental

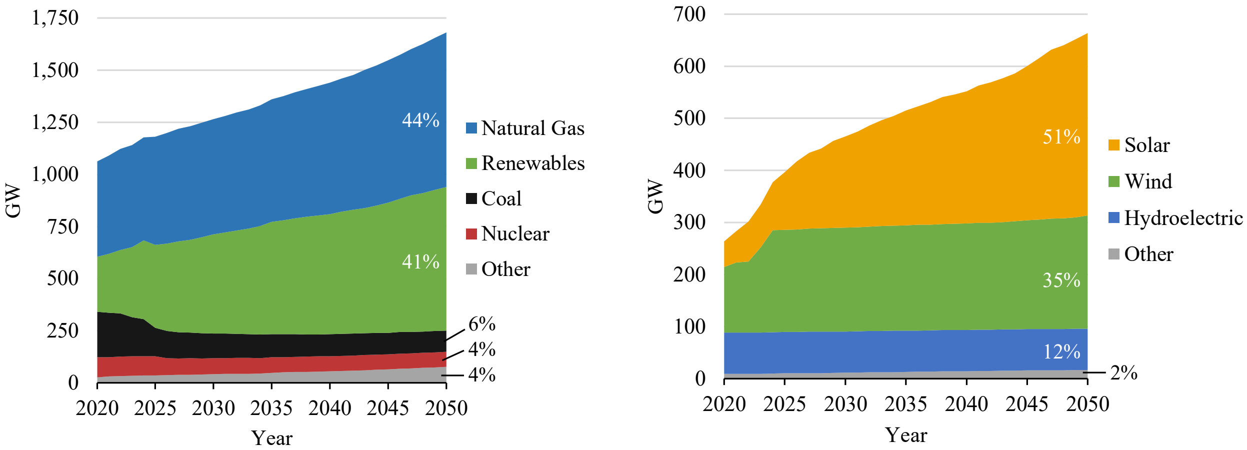

(a) (b)

Fig. 1.2. 2020-2050 projected U.S. electricity generation capacity by type. (a) Total generation capacity. (b) Renewable generation capacity.

solutions, the rapid deployment of additional renewable energy systems on the grid is necessary and expected.

A major challenge to renewable resource penetration is the characteristic intermittency of wind and solar PV generation. These energy sources rely upon wind speed and solar intensity, respectively, and while each typically adheres to a cyclic pattern of availability, the uncertain and irregular nature of renewable resources contrasts with the reliable power dispatch of traditional combustion-based generation [12, 16]. Further, as PV capacity grows, a greater discrepancy is introduced between midday power demand from traditional sources, when solar power is maximized, and late afternoon power demand, when solar power declines. The resulting load schedule, also called the Duck Curve and shown in Fig. 1.3, necessitates dispatchable generation with faster ramping capabilities than previously required [17]. Another challenge of renewable generation is observed in the form of power electronic devices used by distributed energy resources (DERs) to interface with the AC grid. These devices, or voltage source converters (VSCs), lack the rotational momentum of large, centralized generators to maintain grid frequency stability through inertia alone. As the penetration of such modular energy sources and

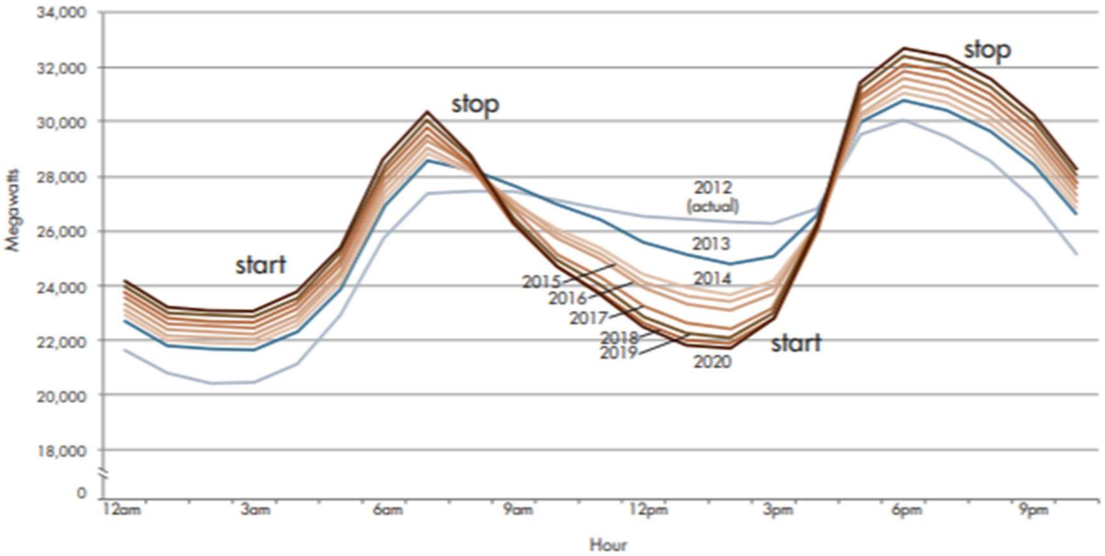

Fig. 1.3. California net electrical load on January 11, 2012-2020. [1]

their corresponding power electronic converters increases, a power electronic-dominated grid (PEDG) may become sustainable at the cost of stability and reliability [18-22].

One solution to overcome the challenges of DERs and realize a resilient PEDG is the deployment of bulk energy storage at the grid edge. Batteries have been proposed as a means of storing excess energy from renewable sources for use during peak load demand. Battery technology, particularly lithium-ion chemistry, has matured rapidly due to the portable consumer electronics market but lacks the production scale and energy density to support the hundreds of gigawatts of new renewable energy capacity needed to replace fossil fuel generation in the coming decades. Deployment of utility-scale battery systems has been limited, in part, due to high costs and short lifetimes. Instead, utility operators typically employ natural gas-powered peaking plants to compensate for any deficiency in bulk or distributed renewable generation. The carbon-based products of natural gas combustion make this a non-ideal solution. A combination of improved energy storage technologies, optimized generation dispatch, and flexible grid topology is needed to best combat DER's various obstacles.

1.2 Voltage source converter operating modes

The power electronic interface between a renewable energy source and its corresponding AC bus is critical for controlling power flow and maintaining stability on the grid. DERs, such as PV panels, require a power electronic interface such as a VSC to transform intermittent generation into an AC sinusoidal waveform compatible with the utility grid [23]. These converters comprise several switching devices and provide a link to the AC bus via an L, LC, or LCL filter to minimize output harmonics [14, 24]. A deeper analysis of these filter designs is presented in later chapters. The following sections provide a brief overview of two primary operating modes for VSCs at grid-edge: grid-following and grid-forming.

1.2.1 Grid-following

A majority of existing distribution-based VSCs operate in a *grid-following* mode, where the power electronics of the VSC track grid voltage to inject a predetermined quantity of active and reactive power [25, 26]. The power setpoints can be optimized to maximize energy output, meet an economic dispatch, support grid frequency, or satisfy another performance objective. In this way, grid-following VSCs act as variable current sources on the utility grid and don't actively support system voltage as its main function [27]. Further, distributed grid-following VSCs are often considered "behind-the-meter" devices that simply reduce the local load seen by utility companies (see Fig. 1.3). Operational flexibility of such devices is limited as they require a grid-energized AC bus to function. However, such DER systems benefit from simple installation and require no energy storage [27]. Control of grid-following VSCs often begins with a phase lock loop (PLL) or frequency integrator for tracking the grid's phase angle. A current reference signal is generated by combining the phase angle with active and reactive power references, often in the *dq* reference frame following a Park transformation [28]. Accurate production of the current reference can be achieved by a variety of control techniques, including classical control schemes such as PI and modulator [28], or advanced mode-based or data-driven strategies such as finite-set model predictive control (MPC) [29-31] and machine learning [32]. By following the grid voltage, these VSCs benefit from simple operation and control but are incapable of operating isolated from the AC grid. Grid-following VSCs comprise a majority of power electronic interfaces to consumer-owned, distribution level DERs.

1.2.2 Grid-forming

PEDG resiliency can be achieved by VSCs that actively support their local bus voltage in voltage-control mode if needed. Such VSCs operate in *grid-forming* mode, where onboard power electronics produce an AC voltage signal from a reference waveform [25-27]. These voltage-controlled devices share the same physical topology (active bridge and filter) as grid-following VSCs but feature active voltage and frequency support that enables islanded operation. When islanded, a grid-forming VSC isolates itself from the utility grid and recreates a voltage reference from an internal lookup table to energize its local bus and supply nearby loads. In this configuration, the VSC acts as a system slack bus and generates only the necessary power to supply local loads at the rated voltage. Alternatively, grid-tied voltage support can be achieved by employing a droop controller to generate a voltage reference from active and reactive power coupled to voltage magnitude and frequency, respectively [33]. The transition between islanded and grid-tied operation is a critical part of the control process and is discussed in detail in later chapters. Some modern VSCs employ hybrid control or "dual-mode" approaches that operate in either current-controlled, grid-following mode or voltage-controlled, grid-forming mode. The transition between operational modes is yet another crucial aspect of the control scheme and will be discussed in later chapters. Similar to grid-following, recreation of the voltage waveform can be realized using PI, MPC, or various other controller architectures [34]. The uncontrolled output power of a grid-forming VSC necessitates the use of battery storage in place of, or supplementing, distributed renewable generation.

1.3 Network of microgrids

The bulk power delivery system built in the nineteenth and twentieth centuries is designed for feeder-style unidirectional power flow from large, centralized power generators to distant, parallelly connected customers [35]. This topology is largely incompatible with a high penetration of DERs and suffers from physical vulnerabilities in the presence of extreme weather or cyber-physical attacks due to lack of observability. Recent advancements in renewable energy systems and the proliferation of modular DERs on the utility grid have created a paradigm shift toward distributed generation and bidirectional power flow. Further, local generation at the grid edge has the potential to enable independent regional operation for increased resiliency. The concept of a *microgrid* has emerged in recent literature as an attractive feature of distributed generation. Specifically, the community microgrid is an emerging technology with the potential to boost grid reliability by utilizing DERs to offer multiple modes of system operation, i.e. islanded or grid-connected mode [2, 27, 34, 36, 37]. The U.S. Department of Energy (DOE) defines microgrid as "a group of interconnected loads and distributed energy resources within clearly defined electrical boundaries that acts as a single controllable entity with respect to the grid. A microgrid can connect and disconnect from the rest of the power grid to enable operation in both grid-connected or islanded mode [38]." The structure of a microgrid allows seamless distribution of renewably generated power among grid clusters. These clusters may comprise cities, neighborhoods, or a few residences, and they offer independent operation by combining DERs with intelligent power electronics. Such an implementation is illustrated in Fig. 1.4 where an interconnected mesh microgrid operates in conjunction with a bulk distribution feeder. Traditional local feeders are also shown for contrast. Here, *mesh* refers to a specific topology in which a generation source may directly tie to three or more other sources, including the utility grid, as opposed to *radial*, in which all generation sources tie to two or fewer other sources [39].

An important characteristic of a microgrid is the ability to seamlessly transition between grid- tied and islanded modes [40]. Ties to the utility grid are useful in default operation when the smaller network can import or export power as needed. In grid-connected mode, many, if not all, VSCs operate in a current-controlled, grid-following mode to meet their respective power references. In the event of damage or an attack disabling the bulk AC power system, the microgrid can shift to islanded operation and supply critical local loads from DERs, including battery storage devices [41, 42]. Islanded operation requires voltage-controlled, grid-forming VSCs to support system voltage in the absence of the utility grid. At minimum, one grid-forming VSCs is necessary, but some control strategies enable power sharing among multiple parallel voltage-controlled sources. In a major deviation from traditional feeder topologies, recent literature has explored microgrids with reconfigurable topologies for even greater robustness and flexibility [43]. Dynamic connections between individual VSCs allow system operators to adapt topology in real time. This is a necessary feature for realizing a network of microgrids, also known as a grid of microgrids or a grid of nanogrids. In addition to individual VSCs synchronizing within a microgrid or nanogrid cluster, modeling of distributed nodes also represents microgrid aggregates within a network of microgrids [44]. In this way, general control

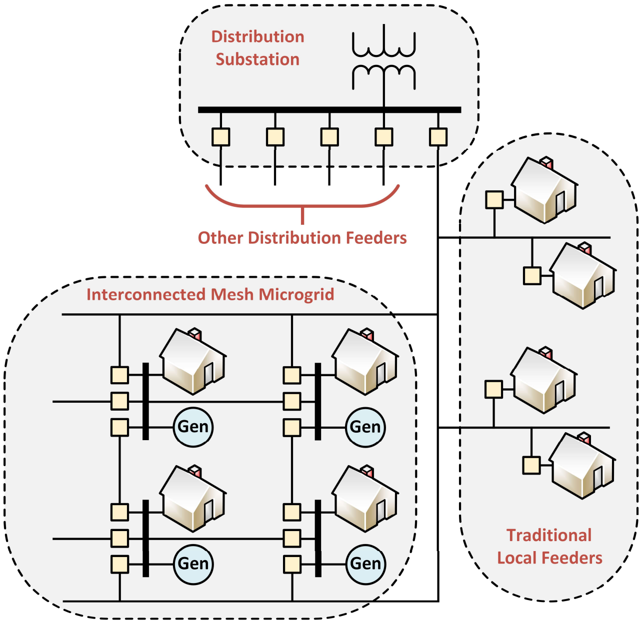

Fig. 1.4. Interconnected mesh microgrid within a traditional distribution network.

structures may apply to VSCs within a grid cluster or grid clusters operating as a single unit within a larger, interconnected system. This new energy paradigm mandates synchronization at multiple points of common coupling.

Two clear limitations arise from such a distributed network: (i) simple VSC controllers may be unable to adapt to changing system configurations within an islanded or grid-tied microgrid, and (ii) islanded operation is reliant upon the inclusion of a grid-forming source to support system voltage [27, 45]. Both limitations highlight concerns of physical topology, and both increase susceptibility to system faults, either on the grid's PCC or at the grid-forming VSC point of connection. Synchronization between distributed generators functioning within the same microgrid or isolated grid clusters presents yet another challenge. Active, voltage-controlled synchronization within an islanded microgrid introduces the risk of conflicting voltage sources unless coordination can be established [46]. The optimal operating mode of each VSC is a function of system configuration. As expanded upon in later chapters, one solution is an adaptive secondary control loop that uses a distributed communication architecture to assign each VSC an appropriate operating mode. The following will explore typical control architectures for VSCs operating within a microgrid topology.

1.3.1 Common microgrid control strategies

Primary and secondary droop controllers have been proposed as solutions to both topology limitations [34, 47, 48]. Droop control enables tunable active and reactive power sharing among distributed VSCs while offering plug-and-play integration. Fig. 1.5(a) shows the characteristic drop in frequency with a corresponding increase in active power generation, compensated for by a change in the nominal frequency. Similarly, Fig. 1.5(b) depicts the drop in voltage magnitude from increased reactive power, compensated for by a change in the nominal voltage magnitude. These controllers eliminate the need for a single grid-forming source by regulating the voltage of every VSC with a secondary control loop. Another benefit of droop control is the lack of traditional centralized communication infrastructure. However, droop control alone is insufficient to support the bidirectional VSC synchronization necessary to achieve seamless transitions between topology configurations. As a partial solution, [49] proposes a consensus-based controller to operate in a dynamic microgrid topology with sparse communication between neighboring VSCs while maintaining power sharing and acceptable voltage regulation. The synchronization for this work is further expanded upon in [50], where leader-follower and distributed averaging methods are implemented to synchronize the islanded microgrid to an external source. This approach is demonstrated to function in various, but limited, system topologies. Specifically lacking, is a solution to synchronization between grid-tied and islanded grid clusters, where leader designation is required on the grid-tied side of the coupling point but lacks a direct tie to the utility grid. Further challenges of droop control include the potential for undesired frequency deviations due to the inherent coupling of the power and voltage reference, as well as transient response time and large-signal stability analysis.

Several recent works have explored the use of MPC with decoupled active and reactive power control to counter the limitations of a typical droop controller [29-31]. As the name

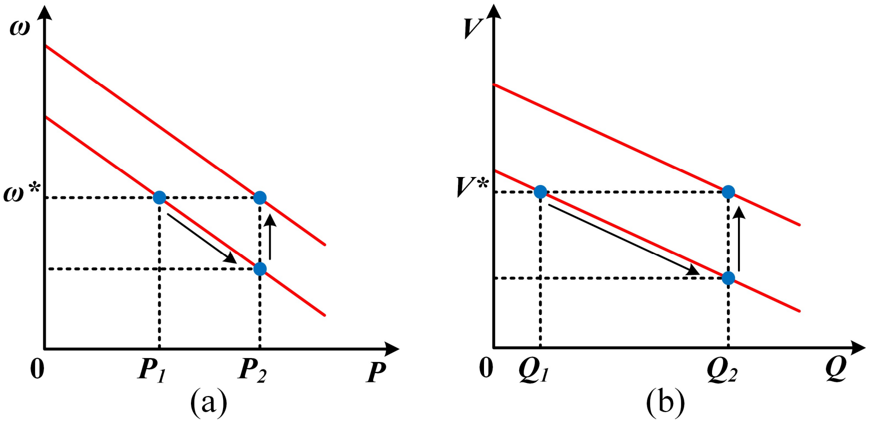

Fig. 1.5. Characteristic droop curves with restoration. (a) P-ω restoration. (b) Q-V restoration [2].

suggests, finite-set MPC leverages a mathematical model of the VSC output filter to predict output current and voltage for each possible switching state. A general dual-objective, three state MPC architecture is shown in Fig. 1.6 [51]. The resulting controller reduces tuning effort, provides single loop design, and offers superior dynamic response [51-55]. The cost function of predictive control allows for multiple possible operation objectives and thus multiple operational modes, such as voltage control or current control. Existing literature investigates MPC techniques for the seamless transition between grid-connected and islanded modes of a microgrid with a single PCC. The authors in [56] present a VSC controller that harnesses MPC to transition between modes by adjusting the control variables' weight factors.

At its most fundamental level, finite-set MPC is a reference tracking tool and can be employed to satisfy any current or voltage reference signal, including those generated from an upper layer droop controller. As discussed in later chapters, this thesis considers current references generated from a Park transformation for decoupled active and reactive power control, and voltage references from measured target waveforms. Without droop curve reference generation, MPC in an islanded microgrid reintroduces the topology limitation of dependence on a voltage controlled, grid-forming source. While most distributed VSCs will meet their power

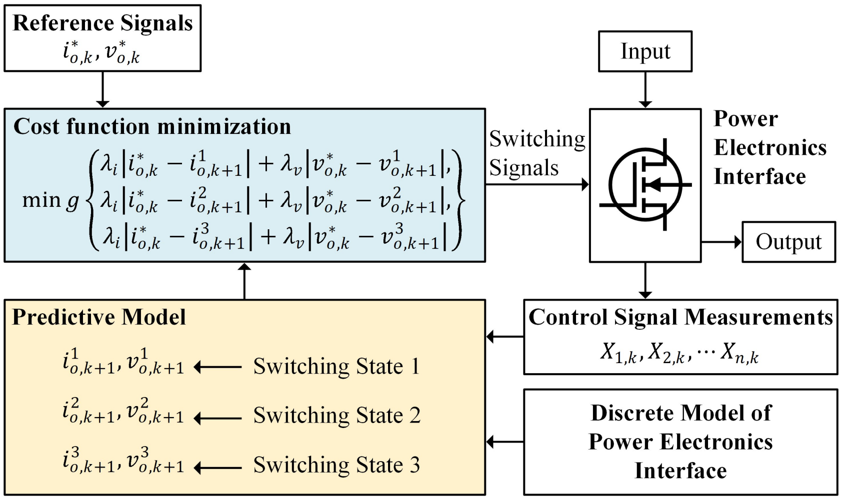

Fig. 1.6. Dual-objective MPC schematic.

references in current control mode, at least one VSC must support system voltage when islanded. This requirement introduces a vulnerability into the microgrid; the voltage collapses without a grid-forming source. To eliminate this weakness and ensure robust performance, the operational mode of each VSC must be adaptable to any network topology. In this way, a single, dual-mode VSC will automatically and seamlessly transition to voltage control mode if the primary grid-forming source is isolated from the remaining islanded microgrid. This transition should take place immediately and without the need for a dense or centralized communication layer between distributed VSCs.

1.4 Microgrid communication architectures

Efficient control of microgrid performance relies on individual VSC operation and coordination among community VSCs. Various levels of communication are necessary for the coordination of many distributed DERs to satisfy performance objectives of varying complexity [57-61]. This communication, whether wired or wireless, requires additional infrastructure. The popularity of droop controllers among researchers is in part due to the communicationless, decentralized plug-and-play nature of the droop curve control strategy [62, 63]. However, communicationless control schemes lack the ability to synchronize waveforms or adapt operational modes based on factors beyond the local bus. Even classical droop controllers require minimal communication infrastructure to remain fully synchronized in every possible microgrid topology. Four communication architectures are explored here and analyzed deeper in later chapters: centralized, multicentralized, distributed, and decentralized [64]. These architectures, shown in Fig. 1.7, are evaluated to determine if they support bidirectional data links between system nodes to enable the complex power sharing, synchronization, and adaptive operation needed in a modern microgrid.

A centralized communication layer employs a single operational point, or hub, with links to every node in the network and is the most common strategy for distributed VSC control. This control architecture is the natural continuation of the modern utility grid's centralized control framework and is easily implemented. A disadvantage of centralized control is its vulnerability to natural disasters or cyber-physical attacks. The central hub represents a strategic target that offers no operational resiliency against a single point of failure [65]. In contrast, a multicentralized communicating layer increases resiliency by designating multiple grid clusters and assigning a central operating node to each. Each cluster behaves as a small centralized layer under the control of a local central operating node. These central nodes further comprise a secondary communication layer for interconnection. The multicentralized strategy prevents total system collapse for any single point of failure by relaying information through local cluster nodes, though each cluster remains individually vulnerable. A distributed communication layer, sometimes referred to as a sparse layer, offers bidirectional peer-to-peer linking between nodes while retaining the limited, localized connections of multicentralization clusters. Distributed control comprises direct connections between a node and its neighbors, such that information passes from one node to another without central processing. Like multicentralized

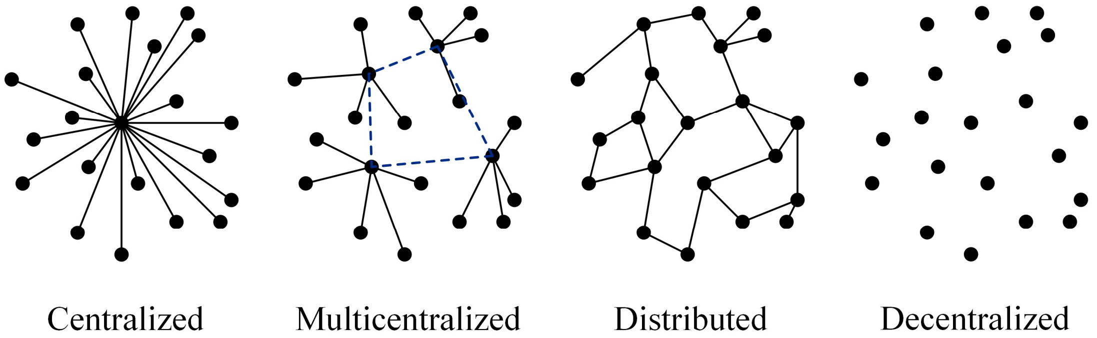

Fig. 1.7. Microgrid communication architectures.

communication, a node communicates only with nearby nodes, thereby limiting the complexity of such a network. The result is a highly robust communication strategy that minimizes vulnerability to system failures while balancing resiliency, practicality, and microgrid flexibility. Finally, a decentralized control adopts a communicationless strategy that provides each node only with measurements from its local bus. An independency of other nodes provides superior resiliency against system faults and failures. This control layer is also the cheapest and simplest to implement, but it lacks the bidirectional communication necessary to coordinate complex and adaptive behaviors among microgrid nodes. Without a level of situational awareness about overall network topology, a node cannot adjust to optimize its performance.

1.5 Network of microgrids with multiple points of common coupling

Recent literature has introduced MPCC as the inevitable culmination of increasing microgrid development and implementation [66-69]. The inclusion of additional coupling points increases the resiliency of grid-tied microgrid operation in three key ways. First, multiple links to the utility grid offer redundancy in the case of PCC failure. A network of microgrids operates most effectively in grid-tied mode where power is imported and exported according to an economic dispatch. While a fundamental characteristic of a microgrid is its ability to island and operate independently, this transition should only occur when necessary, i.e. when the utility grid experiences a fault or collapse, and not amid a PCC hardware failure. Second, MPCC reduces the average physical distance between DER and nearest PCC, which minimizes resistive losses from imported and exported power in distribution lines, thus increasing efficiency. This reduction in physical distance also improves voltage support along the microgrid boundary, and both benefits become more consequential as the size of the microgrid cluster increases. Third, the ability to open and close PCCs at different locations within a network topology provides system operators more flexibility when rerouting power flow and increases import/export capacity. An unexpected surge in exported power may precipitate a PCC line overload, but not if that power is rerouted to higher capacity junctions at the cost of a small efficiency loss. The reverse is also valid, where a PCC is opened to reroute imported power that might otherwise cause a localized overload.

One challenge with MPCC is its implicit bidirectional power flow, in direct opposition to traditional feeder distribution networks. Any PCC junction may be grid-tied at a given instant and topology changes alter the direction of imported or exported power within the microgrid. MPCC prompts the need for adaptable power electronic interfaces to cope with bidirectional power flow and dynamic topologies. Specifically, VSC controllers must acclimate to changing network configurations or performance objectives by actively modifying control parameters. System protection schemes must also be developed for such dynamic topologies where critical power flow setpoints may be dependent on microgrid configuration. An additional challenge of MPCC is internal synchronization encompassing a significant phase shift between electrically distant nodes. These challenges exacerbate those of a single-PCC mesh microgrid and suggest nontrivial solutions.

The exhaustively studied droop controller typically employs a leader/follower approach for synchronization where one VSC at the point of interconnection adjusts its voltage waveform to match its target’s. This method behaves reliably for synchronization to the utility grid at a single PCC, but simultaneous synchronization to multiple coupling points remains largely unexplored. Advanced control schemes have been proposed for increased flexibility of synchronization between two internal nodes but without evidence of optimal performance [49]. Consensus-based controllers require a communication framework to adapt averaging weights to every possible network topology, without which the controllers may perform suboptimal synchronization. Bidirectional power flow is straightforward, as droop controlled VSCs are typically designed for parallel operation [70].

Direct power controllers such as PI or MPC enable explicit operational modes for optimal performance but require communication infrastructure to adapt to topology changes. Synchronization decisions must be made by a centralized controller or via a direct communication link between VSCs in a distributed control layer. The challenge of simultaneous synchronization to MPCC is somewhat alleviated by this communication link but remains an obstacle for a distributed control framework where synchronization may occur far from a PCC. Optimal synchronization can only be achieved when each VSC possesses knowledge of the entire system configuration and can operate accordingly. For these controller types to operate efficiently and resiliently in a microgrid with dynamic topology and MPCC, a secondary control layer must be introduced to enable adaptive operational modes and seamless transitions.

1.5.1 Proposed approach for network of microgrids with MPCC

This thesis presents a rank-based MPC for distributed VSCs operating in a reconfigurable microgrid with dynamic boundaries and MPCC. A ranking scheme is proposed that allows the identity of an islanded microgrid's grid-forming source to adapt autonomously to topology changes, thus providing flexibility to the control structure of the network. The distributed controller allows islanded operation without the primary grid-forming source by delegating grid-forming functionality to another VSC within the system. The ranking algorithm, discussed extensively in later chapters, is applied to each VSC individually as a supervisory layer above a finite-set model predictive controller. It assigns each VSC an operational mode and generates a synchronization reference from an evaluation of surrounding nodes' ranks. To share ranking information, a topology-mirroring distributed communication layer is employed for reliable, local processing that minimizes additional infrastructure. From these ranks, further knowledge of the larger microgrid topology can be determined and inferred upon. Operational transitions are seamless and exhibit robust performance within a microgrid of dynamic topology. The presented rank-based MPC framework results in fully synchronized reconfigurable microgrids that enhance grid resiliency for high renewable energy penetration.

1.6 Preceding publications

This thesis is preceded by two publications of related research that further verify the significance and validity of the presented work. "Enabling Resilient Community Microgrids with Multiple Points of Common Coupling via a Rank-Based Model Predictive Control Framework" has been accepted into the 2021 Applied Power Electronics Conference (APEC) [71]. This paper introduces the rank-based control strategy of this thesis and examines its operation within a three-VSC microgrid topology. Simulated case studies demonstrate the effectiveness of the proposed controller amid network reconfigurations and focus on the adaptive nature of the ranking algorithm.

"Rank-Based Predictive Control Framework for Community Microgrids with Dynamic Reconfigurations and Multiple Points of Common Coupling" has been accepted into the 2021 Power Electronics for Distributed Generation Systems (PEDG) conference [72]. This paper expands upon the rank-based MPC by implementing a six-VSC microgrid with flexible topology in a real-time simulated environment. Furthermore, this paper applies the proposed controller to the problem of black start, in which a fully disconnected and deenergized microgrid network reestablishes local power before synchronizing internally and to the utility grid. The synchronization and subsequent transition of distributed VSCs into an islanded microgrid is explored to validate optimal performance.

1.7 Outline of thesis

This thesis is divided into five chapters. Following this introductory chapter, where an overview of microgrids and VSC control has been presented, Chapter 2 provides an analysis of various VSC filter designs and a derivation of their mathematical models for use in an MPC. A brief overview of filter design is included, followed by a comparative evaluation of topologies using component size, harmonic distortion, and model complexity as performance metrics. The discussion will conclude by selecting an optimal filter design and component values to be applied to microgrid circuits in later chapters.

Chapter 3 presents an in-depth explanation of the proposed rank-based MPC scheme and its use in several microgrid topologies. The controller is systematically compared to traditional control approaches to emphasize its benefits in network with high renewable penetration and changing configurations. Experimental real-time simulation (RTS) case studies follow to demonstrate seamless transition and validate the practical implementation of the proposed ranked predictive controller in a dynamic microgrid with MPCC.

Chapter 4 investigates the scalability of rank-based, distributed controllers in a microgrid environment. Additional system topologies are considered to evaluate the proposed controller when coordinating large mesh groups. Further, this chapter provides an analytical comparison of the four common communication architectures on the basis of communicated distance, cost, and complexity.

Finally, Chapter 5 presents a future research roadmap and concluding remarks about the proposed rank-based control scheme and its use in topologies with multiple coupling points to the utility grid. The direction of future research is discussed with respect to an increasingly sustainable, distributed, and dynamic power system.

Chapter 2 - Model Predictive Control of Voltage Source Converters and Filter Evaluation

2.1 Filters in voltage source converters

As previously mentioned, a VSC interfaces with a local AC bus via an output lowpass filter. The purpose of this filter is to extract the fundamental components of the current and filter out harmonics caused by the high frequency switching. IEEE standard 519 provides an upper limit to voltage and current harmonic content within various grid systems [73]. The most common filter topologies, L, LC, and LCL, shown in Fig. 2.1 have been used extensively in literature and commercial products, and each present their own benefits and challenges. MPC takes advantage of the differential characteristics of the reactive elements to predict the system's state variables, and by extension, the optimal switching states for finite control. A complete description of finite-set MPC operation is provided in later sections. In the following, the mathematical models for each of the three typical filter topologies will be derived and discretized for use in a single-phase, discrete predictive controller. The filters will then be further compared on the basis of performance and operational viability.

2.2 Mathematical model and discretization

Derivation of the discrete, predictive model begins with the dynamic model equations governing the voltage across an inductor and flow of current through a capacitor. These expressions are then solved for inductor current and capacitor voltage time derivatives, the

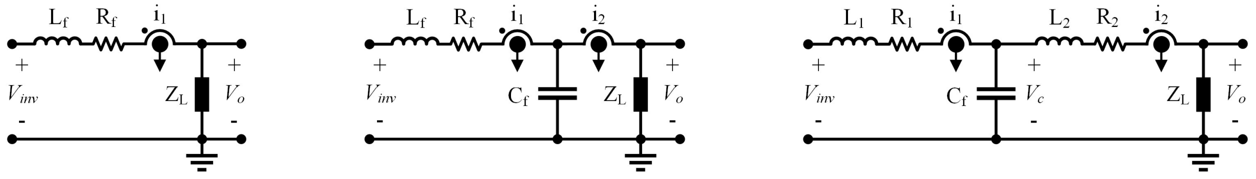

(a) (b) (c)

Fig. 2.1. Common filter topologies. (a) L filter. (b) LC filter. (c) LCL filter.

system state variables. The single-phase model is discretized and used to predict step-ahead converter voltage and current, when possible. These predicted values are applied to the MPC cost function in later chapters to satisfy voltage and current references.

2.2.1 L filter model

The dynamic model of the single-phase L filter is given by (2.1) where L_f is the value of the inductor and R_f is the value of its equivalent series resistance (ESR). The state space representation for this continuous-time system is given by (2.2) where system coefficients A and B are defined by (2.3).

$$\frac{di_1}{dt} = \frac{1}{L_f}\left[v_{inv} - i_1 R_f - v_o\right] \tag{2.1}$$

$$\frac{d}{dt}\left[i_{1,k}\right] = A\left[i_{1,k}\right] + B\begin{bmatrix} v_{inv,k} \\ v_{o,k} \end{bmatrix} \tag{2.2}$$

$$A = \left(-\frac{R_f}{L_f}\right) \qquad \text{and} \qquad B = \left(\frac{1}{L_f} \quad -\frac{1}{L_f}\right) \tag{2.3}$$

The system is then discretized by applying a zero-order hold with time step T_s and solved for the step-ahead estimations using (2.4) where coefficients A_d and B_d are defined using their continuous counterparts in (2.5) [74, 75]. Notably, (2.4) allows for the estimation of output current $i_{1,k+1}$ and thus power reference tracking in current-control mode can be achieved with MPC. However, this equation does not provide an expression for predicted output voltage, thus voltage-controlled operation is not possible with only an L filter.

$$\left[i_{1,k+1}\right] = A_d\left[i_{1,k}\right] + B_d\begin{bmatrix} v_{inv,k} \\ v_{o,k} \end{bmatrix} \tag{2.4}$$

$$A_d = e^{AT_s} \qquad \text{and} \qquad B_d = \int_0^{T_s} e^{A\tau} B\, d\tau = \left[\frac{e^{A\tau}}{A}\right]_0^{T_s} B = A^{-1}\left(A_d - I\right)B \tag{2.5}$$

2.2.2 LC filter model

The dynamic model of inductor current in the single-phase LC filter is equivalent to (2.1). The dynamic model of capacitor voltage is given by (2.6) where C_f is the value of the output filter capacitor. The state space representation for this second-order, continuous-time system is given by (2.7) where system coefficients *A* and *B* are defined by (2.8).

$$\frac{dv_o}{dt}=\frac{1}{C_f}\left[i_1-i_2\right] \tag{2.6}$$

$$\frac{d}{dt}\begin{bmatrix} i_{1,k} \\ v_{o,k} \end{bmatrix}=A\begin{bmatrix} i_{1,k} \\ v_{o,k} \end{bmatrix}+B\begin{bmatrix} v_{inv,k} \\ i_{2,k} \end{bmatrix} \tag{2.7}$$

$$A=\begin{pmatrix} -\frac{R_f}{L_f} & -\frac{1}{L_f} \\ \frac{1}{C_f} & 0 \end{pmatrix} \quad \text{and} \quad B=\begin{pmatrix} \frac{1}{L_f} & 0 \\ 0 & -\frac{1}{C_f} \end{pmatrix} \tag{2.8}$$

The system is then discretized by applying a zero-order hold with time step T_s and solved for the step-ahead estimations using (2.9) where coefficients A_d and B_d are defined using their continuous counterparts from the formulation in (2.5). (2.9) provides step-ahead predictions for bridge-side current and output voltage, but more accurate power tracking can be achieved by predicting output current, $i_{2,k+1}$. An estimation for the output current can be calculated by applying KCL at the output node (2.10). The prediction of both output current and voltage enables grid-following and grid-forming operational modes.

$$\begin{bmatrix} i_{1,k+1} \\ v_{o,k+1} \end{bmatrix}=A_d\begin{bmatrix} i_{1,k} \\ v_{o,k} \end{bmatrix}+B_d\begin{bmatrix} v_{inv,k} \\ i_{2,k} \end{bmatrix} \tag{2.9}$$

$$i_{2,k+1}=i_{1,k+1}-C_f\left(\frac{v_{o,k+1}-v_{o,k}}{T_s}\right) \tag{2.10}$$

2.2.3 LCL filter model

The dynamic model of the single-phase LCL filter is given by (2.11)-(2.13) where L_1 and R_1 are the inductance and ESR of the first inductor, respectively, and L_2 and R_2 are the inductance and ESR of the second inductor, respectively [76, 77]. C_f represents the value of the filter capacitor. The state space representation for this third-order, continuous-time system is given by (2.14) where system coefficients *A* and *B* are defined by (2.15).

$$\frac{di_1}{dt}=\frac{1}{L_1}\left[v_{inv}-i_1R_1-v_c\right] \tag{2.11}$$

$$\frac{dv_c}{dt}=\frac{1}{C_f}\left[i_1-i_2\right] \tag{2.12}$$

$$\frac{di_2}{dt}=\frac{1}{L_2}\left[v_c-i_2R_2-v_o\right] \tag{2.13}$$

$$\frac{d}{dt}\begin{bmatrix} i_{1,k} \\ v_{c,k} \\ i_{2,k} \end{bmatrix}=A\begin{bmatrix} i_{1,k} \\ v_{c,k} \\ i_{2,k} \end{bmatrix}+B\begin{bmatrix} v_{inv,k} \\ v_{o,k} \end{bmatrix} \tag{2.14}$$

$$A=\begin{pmatrix} -\frac{R_1}{L_1} & -\frac{1}{L_1} & 0 \\ \frac{1}{C_f} & 0 & -\frac{1}{C_f} \\ 0 & \frac{1}{L_2} & -\frac{R_2}{L_2} \end{pmatrix} \quad \text{and} \quad B=\begin{pmatrix} \frac{1}{L_1} & 0 \\ 0 & 0 \\ 0 & -\frac{1}{L_2} \end{pmatrix} \tag{2.15}$$

The system is discretized by applying a zero-order hold with time step T_s and solved for the step-ahead estimations in (2.16) where coefficients A_d and B_d are defined using their continuous counterparts using the same formulation in (2.5). The converter side current will be used in the MPC algorithm for stable control of output power, and an expression for the estimated step-ahead output voltage $v_{o,k+1}$ can be calculated from KVL around the output loop (2.17). Thus, both grid-following and grid-forming modes of operation are viable.

$$\begin{bmatrix} i_{1,k+1} \\ v_{c,k+1} \\ i_{2,k+1} \end{bmatrix}=A_d\begin{bmatrix} i_{1,k} \\ v_{c,k} \\ i_{2,k} \end{bmatrix}+B_d\begin{bmatrix} v_{inv,k} \\ v_{o,k} \end{bmatrix} \tag{2.16}$$

$$v_{o,k+1}=v_{c,k+1}-i_{2,k+1}R_2-L_2\left(\frac{i_{2,k+1}-i_{2,k}}{T_s}\right) \tag{2.17}$$

2.3 MPC operation and reference generation

A finite-set model predictive controller utilizes the output voltage and current step-ahead estimations derived previously to directly select an optimal switching pattern at each time step.

This is accomplished with a cost function for minimizing system errors and undesired performance metrics. The implementation of multiple operational objectives is a major advantage of MPC, as well as its fast dynamic response and simplicity. A cost function g is presented in (2.18) to minimize the errors between a VSC's estimated step-ahead output parameters and their respective references, where λ_i and λ_v are current and voltage weight factors, respectively. These binary weight factors determine the operating mode of the VSC, and their assignment in the proposed controller is detailed in future chapters.

$$g = \lambda_i \left| i^*_{o,k} - i_{o,k+1} \right| + \lambda_v \left| v^*_{o,k} - v_{o,k+1} \right| \tag{2.18}$$

Because the step-ahead estimations for output current and voltage are dependent on the instantaneous VSC bridge output voltage v_{inv}, the prediction calculations are performed for each possible switching state. For a 2-level, single phase bridge, the three viable switching states result in instantaneous v_{inv} values of V_{dc}, $-V_{dc}$, and 0. Thus, three predictions are made at each time step, and the switching state that minimizes the cost function is selected.

2.3.1 Current reference generation

In current-control mode, $\lambda_i = 1$ and $\lambda_v = 0$. Current reference $i^*_{o,k}$ is generated from equations (2.19)-(2.24) to decouple and regulate active and reactive power output in current-control mode, as depicted in Fig. 2.2. First, a second-order generalized integrator (SOGI) is employed to create orthogonal signals of the PCC voltage, v_o, in the $\alpha\beta$ reference frame. The transfer functions of the SOGI module are given by (2.19), and the resulting orthogonal signals are included in (2.20). A Park transformation in (2.21) produces dq components of the PCC voltage, where phase angle $\theta_{o,k}$ is generated by integrating the nominal output frequency ω_n. The single-phase active and reactive power references in the dq frame are given by (2.21) and rearranged to solve for the dq current reference components in (2.23). Finally, the time-variant current reference is generated by (2.24).

$$\frac{v_{o-\alpha}(s)}{v_o(s)} = \frac{\omega s}{s^2 + \omega s + \omega^2} \quad \text{and} \quad \frac{v_{o-\beta}(s)}{v_o(s)} = \frac{\omega^2}{s^2 + \omega s + \omega^2} \tag{2.19}$$

$$v_{o-\alpha} = v_o \sin(\omega t) \quad \text{and} \quad v_{o-\beta} = v_o \sin\left(\omega t + \frac{\pi}{2}\right) \tag{2.20}$$

$$v_{o-d,k} = v_{o-\alpha,k} \sin(\theta_{o,k}) - v_{o-\beta,k} \cos(\theta_{o,k}) \quad \text{and} \quad v_{o-q,k} = v_{o-\alpha,k} \cos(\theta_{o,k}) + v_{o-\beta,k} \sin(\theta_{o,k}) \tag{2.21}$$

$$P_k^* = \frac{1}{2}\left(v_{o-d,k} i_{o-d,k}^* + v_{o-q,k} i_{o-q,k}^*\right) \quad \text{and} \quad Q_k^* = \frac{1}{2}\left(v_{o-q,k} i_{o-d,k}^* - v_{o-d,k} i_{o-q,k}^*\right) \tag{2.22}$$

$$i_{o-d,k}^* = \frac{2\left(P_k^* v_{o-d,k} + Q_k^* v_{o-q,k}\right)}{v_{o-d,k}^2 + v_{o-q,k}^2} \quad \text{and} \quad i_{o-q,k}^* = \frac{2\left(P_k^* v_{o-q,k} - Q_k^* v_{o-d,k}\right)}{v_{o-d,k}^2 + v_{o-q,k}^2} \tag{2.23}$$

$$i_{o,k}^* = i_{o-d,k}^* \sin\theta_{o,k} + i_{o-q,k}^* \cos\theta_{o,k} \tag{2.24}$$

2.3.2 Voltage reference generation

In voltage-control mode, $\lambda_i = 0$ and $\lambda_v = 1$. The MPC algorithm compares voltage reference $v^*_{o,k}$ to the predicted step-ahead voltage signal. The generation of this voltage reference depends on the scenario in which a VSC enters this mode. If the VSC is operating as a grid-forming source within an islanded microgrid, $v^*_{o,k}$ is generated from an internal lookup table containing the values of an optimal sinusoid signal of rated frequency and amplitude. In the case of synchronization, the voltage reference is provided by a local measurement at the far side of the switch isolating the synchronizing VSC from its target bus. A synchronizing VSC observes its target waveform from the bus and $v^*_{o,k}$ is slowly adapted to the new signal. A seamless shift in output voltage occurs as the controller steadily alters the phase angle and voltage magnitude of

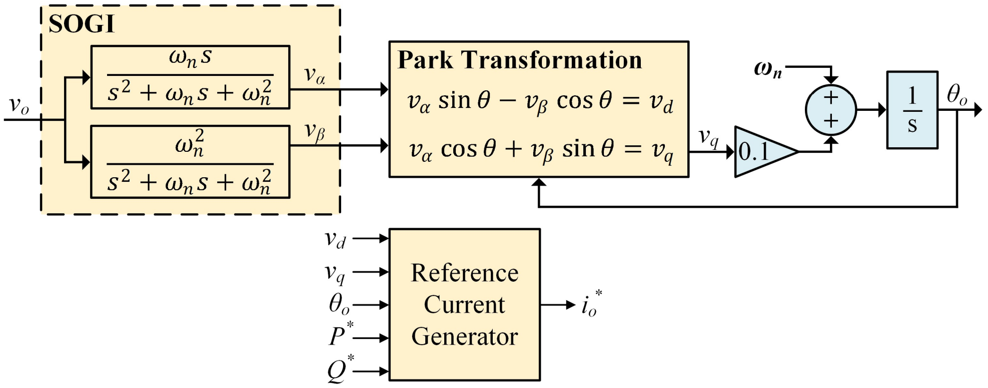

Fig. 2.2. Reference current generation.

$v^*_{o,k}$ to match the target waveform. In this way, all reference signals are generated on-device using only local measurements for decentralized control.

2.4 Filter comparison and frequency analysis

Filter design plays an important role in the performance, control, and cost of a VSC. To compare the three common topologies, the operation of each is inspected under identical test conditions with an appropriate predictive controller within a Simulink circuit model. This case study comprises of L, LC, and LCL filters behaving as interfaces between identical single-phase bridges and a common AC grid. Each VSC testbed is supplied by a DC source and alternates between islanded mode, where a voltage reference is met to supply a local load, and grid-tied mode, where a power reference is satisfied and excess power is exported to the grid. Constant circuit parameters are listed in Table 2.1, which remain the same between studies. Table 2.2 contains the results of six case studies where output voltage harmonic content (THD_v) is examined for each filter under current-control and voltage-control operating modes. Similarly, Table 2.3 contains the results of six case studies where output current harmonic content (THD_i) is examined for each filter under current-control and voltage-control operating modes. The filter

Table 2.1. Constant circuit parameters for filter comparison.

Parameter	**Value**
DC link voltage V_{DC}	200V
Sample time T_S	20μs
Inductor ESR (each) R_f	10mΩ
Local load R_L	5Ω
Active power reference P^*	5kW
Reactive power reference Q^*	1kVAR
Grid line impedance Z_G	(10+j0.1)mΩ
Rated grid voltage V_G	$100V_{pp}$
Rated grid frequency f_G	60Hz

Table 2.2. Filter voltage THD comparison case studies and results.

Topology	**Control Mode**	**L_1**	**C_f**	**L_2**	**THD_v**	**Active Power Accuracy**
L	Current	5mH	▨	▨	1.0%	93.0%
LC	Current	13mH	10µF	▨	1.0%	12.7%
LCL	Current	2mH	10µF	0.1mH	1.0%	12.3%
L	Voltage	▨	▨	▨	▨	▨
LC	Voltage	4mH	10µF	▨	1.0%	▨
LCL	Voltage	20mH	10µF	0.05mH	1.0%	▨
L	Current	1.8mH	▨	▨	3.0%	99.8%
LC	Current	4.8mH	10µF	▨	3.0%	94.4%
LCL	Current	0.8mH	5µF	0.05mH	3.0%	99.4%
L	Voltage	▨	▨	▨	▨	▨
LC	Voltage	1.4mH	10µF	▨	3.0%	▨
LCL	Voltage	7mH	5µF	0.05mH	3.0%	▨
L	Current	1mH	▨	▨	5.0%	99.6%
LC	Current	3.2mH	10µF	▨	5.0%	99.1%
LCL	Current	0.4mH	5µF	0.05mH	5.0%	99.3%
L	Voltage	▨	▨	▨	▨	▨
LC	Voltage	0.8mH	10µF	▨	5.0%	▨
LCL	Voltage	4.5mH	5µF	0.05mH	5.0%	▨

component sizes required to realize the target THD limits are listed for comparison, as well as active power tracking accuracy.

2.4.1 Case study discussion

Several patterns emerge from the results of Table 2.2 and Table 2.3. In general, the harmonic content of the output voltage and current waveforms increases as the size of the primary inductor decreases. This is especially true for current-controlled operation, highlighted in gray, where a larger inductor helps to smooth the output current for better harmonic attenuation. Similarly, an increased capacitor size correlates to a reduction in voltage harmonic

Table 2.3 Filter current THD comparison case studies and results.

Topology	**Control Mode**	**L_1**	**C_f**	**L_2**	**THD_i**	**Active Power Accuracy**
L	Current	1.7mH	▨	▨	1.0%	99.8%
LC	Current	4.2mH	5μF	▨	1.0%	99.5%
LCL	Current	1.1mH	5μF	0.05mH	1.0%	99.6%
L	Voltage	▨	▨	▨	▨	▨
LC	Voltage	4mH	10μF	▨	1.0%	▨
LCL	Voltage	20mH	10μF	0.05mH	1.0%	▨
L	Current	0.6mH	▨	▨	3.0%	99.4%
LC	Current	1.6mH	5μF	▨	3.0%	98.5%
LCL	Current	0.3mH	5μF	0.025mH	3.0%	99.2%
L	Voltage	▨	▨	▨	▨	▨
LC	Voltage	1.4mH	10μF	▨	3.0%	▨
LCL	Voltage	7mH	5μF	0.05mH	3.0%	▨
L	Current	0.3mH	▨	▨	5.0%	99.1%
LC	Current	1.0mH	5μF	▨	5.0%	97.4%
LCL	Current	0.2mH	5μF	0.025mH	5.0%	99.0%
L	Voltage	▨	▨	▨	▨	▨
LC	Voltage	0.8mH	10μF	▨	5.0%	▨
LCL	Voltage	4.5mH	5μF	0.05mH	5.0%	▨

content, but also to an increase in current harmonic content. The accuracy of power tracking correlates directly to inductor size and inversely to capacitor size.

Table 2.2 includes the necessary filter component sizes to achieve THD_v targets of 1%, 3%, and 5%. In grid-tied, current-control mode (gray), the LC design requires larger components than either the L or LCL filters to contain the same levels of THD_v. Specifically, the LC filter inductor is approximately 3x larger than the L filter inductor, and approximately 6x larger than the primary inductor found in the LCL design. However, in voltage-control mode (white), the LC filter requires an inductor approximately 5x *smaller* than the primary LCL inductor at every THD_v level. The L filter is unable to operate in voltage-control mode, regardless of component size. Superior active power tracking in current-control mode is achieved by the L filter, though the LC and LCL designs follow closely behind. The exception is the 1% THD_v study where LC and LCL component sizes are sufficiently large to destabilize power tracking.

Table 2.3 includes the necessary filter component sizes to achieve THD_i targets of 1%, 3%, and 5%. The conclusions made from Table 2.2 regarding relative component sizes in current-control and voltage-control modes hold true here, where the LC filter suffers in current-control mode but outperforms the LCL design in voltage-control mode. In general, the components required to achieve any THD_i in Table 2.3 are smaller in current-control mode and identical in voltage-control mode, to those necessary for an equivalent THD_v in Table 2.2.

The L filter offers some advantages over more complex designs. First, the simplicity of its model allows the MPC algorithm to produce very little computational burden when calculating step-ahead estimations. Second, harmonic content of the current waveform is minimal when the VSC is operating in current-control mode, performing comparably to the LCL filter in most case studies. Active power tracking accuracy also matches or exceeds that of the LCL filter. Despite these advantages, the L filter suffers a critical flaw in the VSC's inability to operate in voltage-control mode, regardless of controller architecture. Limiting VSC operation to current-controlled applications is a severe drawback as the controller proposed in this thesis relies on the adaptability of VSC operating modes. Fixed-mode converters, while simpler in design and implementation, do not offer the flexibility or resiliency required for dynamic, mesh microgrids.

In contrast, the LC filter with its output capacitor, is capable of voltage-controlled operation, where it offers superior harmonic attenuation in both the voltage and current waveforms. In every voltage-control case study, the LC filter inductor required to achieve target harmonic content is approximately 5x smaller than the primary LCL inductor. This is due to the LC filter's output capacitor tied directly to the output bus for better voltage control. However, current-controlled performance suffers as a result, based on both harmonic distortion and power tracking accuracy.

The LCL filter's performance is inverse that of the LC. With an additional inductor to smooth output current, the harmonic content of both voltage and current is minimized in current-control mode. In every grid-tied, current-controlled case study where an appropriately sized output inductor is applied, the LCL filter necessitates smaller component sizes than those of similarly performing L and LC filters. Power reference tracking is similar to that of the L filter. Voltage-controlled operation, however, results in significant harmonic content on the voltage and current waveforms due to the LCL's capacitor sitting behind an output inductor. An additional consideration of the LCL filter is the computational burden of estimating step-ahead state variables for the third-order system. Simpler filter topologies benefit from fewer MPC computational requirements.

2.4.2 Frequency analysis

In addition to enabling dual-mode operation among MPC-equipped VSCs, the LC and LCL topologies are often valued for their precise attenuation of high frequency harmonics. However, control of these filter designs is somewhat complicated by the presence of natural resonance frequencies between the dynamic components. The LC filter experiences a single resonance frequency with an inverse dependency on inductor size, as is evident in the Bode plots of Fig. 2.3. The filter capacitor is set to 10μF. Fig. 2.3(a) and Fig. 2.3(b) show the magnitude response of the LC filter's state variables, converter-side current and output voltage, with respect to VSC bridge voltage. The resonance frequencies between inductor and capacitor that are visible in both plots can create stability challenges if not properly considered. It is difficult to estimate the average switching frequency of the predictive controller, but at a sampling rate of 50kHz, high frequency harmonics are likely to be well above the depicted resonance frequencies and thus will be attenuated appropriately.

The LCL filter presents similar magnitude responses for its state variables, converter-side current, capacitor voltage, and grid-side current with respect to VSC bridge voltage. Here, the filter capacitor and converter-side inductor are set to 10μF and 3mH, respectively. Fig. 2.4 depicts the same inverse relationship between resonance frequency and inductor size. However, unlike the LC filter, this frequency evaluation is performed by changing the grid-side inductor, L_2. Two resonance frequencies are present in the LCL filter, as is evident by the magnitude

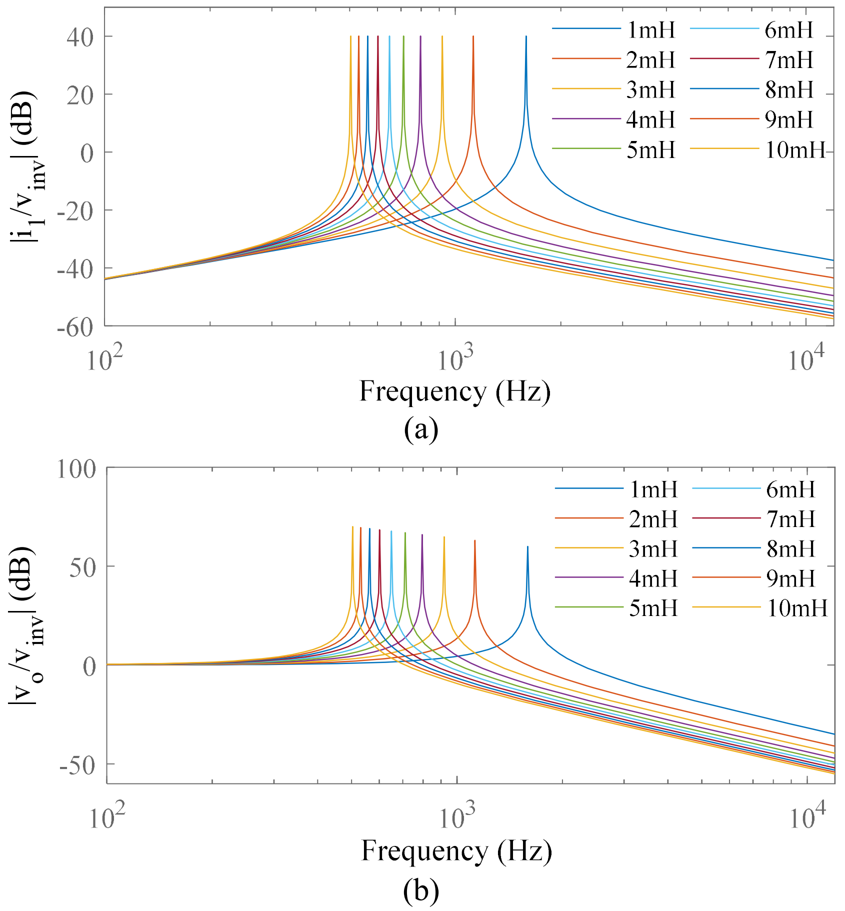

(a)

(b)

Fig. 2.3. Bode plot of LC filter system with changing inductor. (a) Inductor current i_1 with respect to bridge voltage. (b) Output voltage v_o with respect to bridge voltage.

response of converter-side current, shown in Fig. 2.4(a). These resonance frequencies are products of the two inductors in the filter circuit, and the difference between them grows as L_2 increases. Fig. 2.4(b) and Fig. 2.4(c) depict the magnitude response of capacitor voltage and

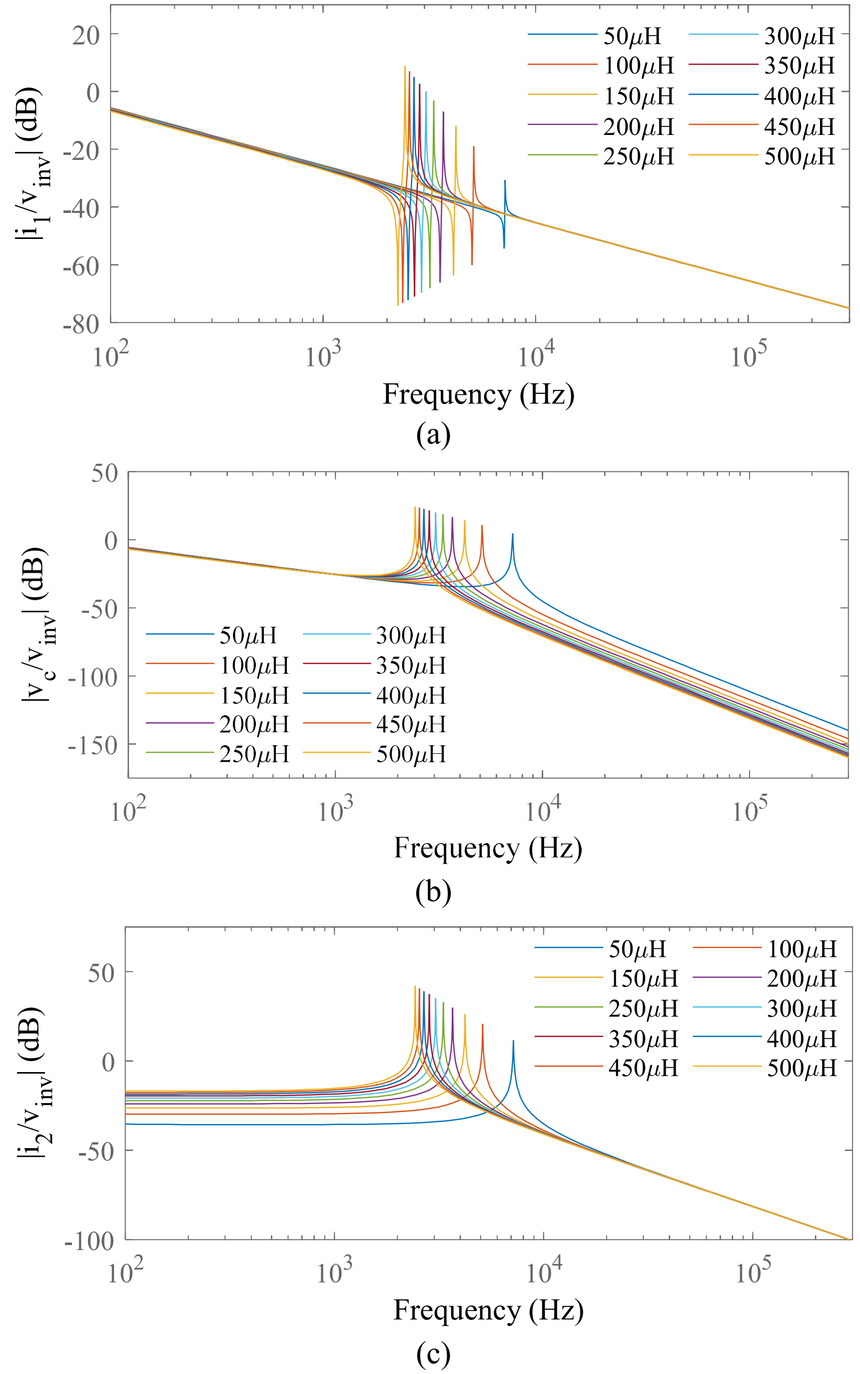

Fig. 2.4. Bode plot of LCL filter system with changing output inductor. (a) Converter-side inductor current i_1 with respect to bridge voltage. (b) Capacitor voltage v_c with respect to bridge voltage. (c) Grid-side inductor current i_2 with respect to bridge voltage.

grid-side current, respectively. As with the LC filter, the resonance frequencies present in the LCL design are well below the expected average switching frequency of the converter and can be easily avoided. However, the LCL resonance frequencies are considerably higher than those of the LC filter and present a more challenging control problem.

2.5 Filter selection

In later chapters, a microgrid testbed will comprise many distributed finite-set MPC VSCs with identical filters to demonstrate the proposed controller's functionality. While a real-world implementation could include multiple filter designs for optimized performance, identical filters permit simpler operation verification and performance comparisons between neighboring VSCs. As such, a single filter design must be selected that offers both voltage-control and current-control operational modes. This prerequisite disqualifies the simple L filter due to its lack of voltage controllability.

A comparison between the remaining LC and LCL filters includes an evaluation of performance metrics, hardware requirements, and frequency analysis. The LCL design benefits from smaller necessary component sizes in current-control mode and thus a potentially smaller footprint, but the LC design presents a simpler topology and reduced computational burden on the MPC algorithm. The LC filter also benefits from superior harmonic content with smaller component sizes in voltage-control mode. The proposed rank-based controller ensures most distributed VSCs operate in current-control mode within a microgrid topology, where the LCL filter's performance would advantageous. However, as the controller assigns just one voltage-controlled, grid-forming source within an islanded network, the voltage-control performance of that VSC is critical for island voltage support. Further, the careful tuning requirements and stability challenges of the LCL filter contribute to a higher difficulty of implementation. For these reasons, the LC filter design is selected for future microgrid case studies. An inductor size of 3mH and a capacitor size of 10μF will be used to balance the output harmonic content with reference power tracking and physical hardware size. According to Table 2.2 and Table 2.3, these component sizes will keep operating harmonics well within the limits outlined by IEEE standard 519 [73].

Chapter 3 - Rank-Based Model Predictive Controller for Community Microgrids with MPCC

3.1 MPC ranking scheme

As discussed in previous chapters, a higher margin of resiliency and flexibility can be achieved with a microgrid cluster of dual-mode VSCs. Adaptive operational modes enable optimal performance amid changing topology and dynamic boundaries by assigning voltage-control and current-control status among distributed VSCs to suit a given network configuration. This can be accomplished by exploiting the multi-objective cost function of a model predictive controller, where locally generated weight factors define the operational mode of each VSC. The resulting fully synchronized control structure offers superior performance and robustness with flexible boundaries and MPCC.

Fig. 3.1 depicts the proposed control structure. An adaptive ranking scheme is implemented to facilitate the distributed control of clustered, single-phase VSCs within a mesh microgrid. Limited communication between neighboring converters provides information about the surrounding topology, and each VSC controller generates corresponding weight factors to

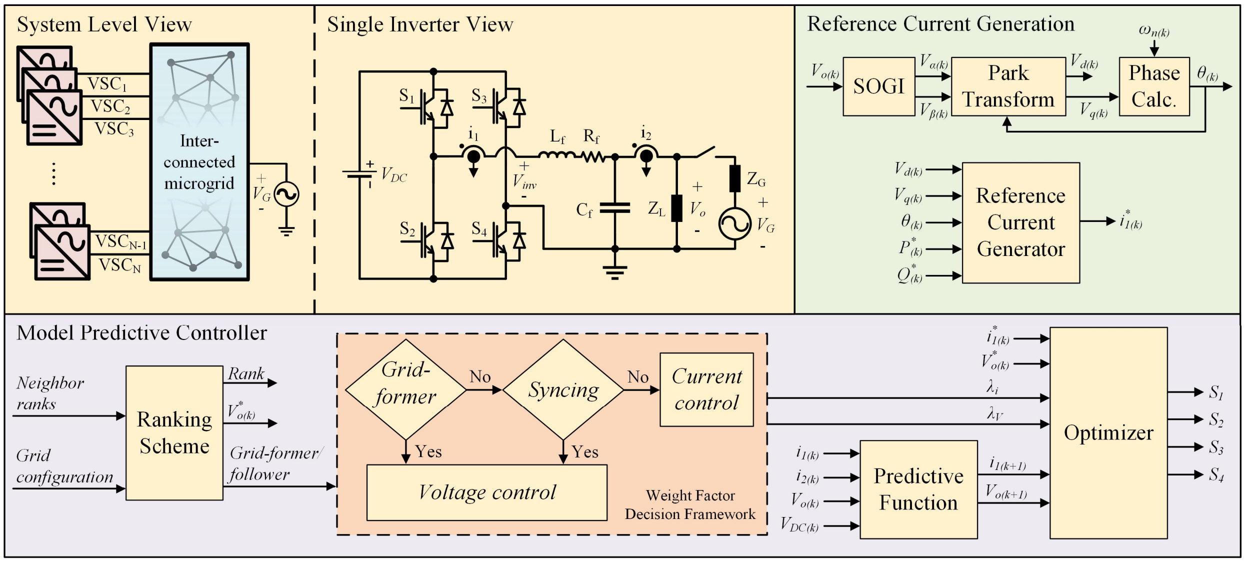

Fig. 3.1. Proposed system configuration

govern operational mode. A grid-forming/following approach is implemented in the proposed controller where exactly one VSC in an islanded system operates in voltage-control mode and behaves as the central point of synchronization. If grid-tied, all VSCs operate in current-control mode and follow the utility grid's waveform. The VSC(s) at a PCC to the utility grid behaves as a central reference of synchronization.

The operational mode of each VSC is determined by its rank R and the ranks of neighboring, tied VSCs. Ranks are conveyed between neighboring VSCs and are the only pieces of information shared between buses via the sparse communication layer. Each VSC begins with a unique integer ID to differentiate it from other VSCs in the system and create a predefined control structure within an islanded microgrid. Considering the i^{th} VSC, a constant, unique initial rank $R_{o,i}$ is then derived using (3.1), where N is the maximum number of total VSCs within the microgrid. The application of (3.1) ensures at least N-1 integer ranks between VSC_i and any tied neighbor. The final rank of VSC_i, R_i, is dependent on the initial rank $R_{o,i}$, the binary state of the utility tie to the i^{th} local bus G_i, and the ranks of n neighboring, tied VSCs. The rank R_i at time

Algorithm I: VSC ranking scheme and weight factor determination

```
Initialization: $B=[B_1\ B_2 \dots B_M]_{1xM}$, $T=[T_1\ T_2 \dots T_M]_{1xM}$, ID=ID;
1:Initial rank formulation
  $R_o \leftarrow ID*N$
2:Rank assignment
  If ($G = 1$)
    $R \leftarrow 1$
    $\lambda_i \leftarrow 1$
    $\lambda_V \leftarrow 0$ , grid-tied and current-control mode
  Else
    $R \leftarrow R_o$
    $\lambda_i \leftarrow 0$
    $\lambda_V \leftarrow 1$ , islanded and voltage-control mode
     For ($j = 1:M$)
       If ($T(j)==1$ && $B(j) < R$)
          $R \leftarrow B(j) + 1$
          $\lambda_i \leftarrow 1$
          $\lambda_V \leftarrow 0$ , islanded and current-control mode
       end if
     end for
  end if
```

step k is given by (3.2), where T_{ij} is the binary tie command for a line between buses i and j, and B_j is the rank of the j^{th} VSC. The rank assignment process is further explained by Algorithm I.

$$R_{o,i} = (ID)_i \times N \tag{3.1}$$

$$R_{i,k} = G_{i,k} + \min_{j=0:n}\left[T_{ij,k}\left(B_{j,k-1}+1\right) + R_{o,i}\left(1-T_{ij,k}\right)\right]\left(1-G_{i,k}\right) \tag{3.2}$$

A comparison of VSC$_i$'s rank R_i to the ranks of its neighbors determines its operational mode. If R_i is less than the ranks of neighboring, tied VSCs, $R_i=R_{o,i}$, and VSC$_i$ operates in voltage-control mode. Otherwise, R_i equals the rank of VSC$_i$'s least-ranking tied neighbor incremented by one, and VSC$_i$ operates in current-control mode. The only exception to this rule applies to grid-tied VSCs, which are assigned the lowest possible rank of 1 and always operate in current control mode. This eliminates the possibility of a grid-tied VSC synchronizing to a different VSC within the system and ensures that the direction of synchronization at any point within a grid-tied microgrid is always toward the nearest PCC. In this way, multiple VSCs within the microgrid can tie or untie to the same utility grid seamlessly. As the topology of the microgrid changes, ranks automatically adapt to guarantee one voltage-controlled source in an islanded system and zero voltage-controlled sources in a grid-tied system. Each VSC synchronizes to its least-ranking tied neighbor, forming a chain of connected VSCs whose ranks grow consecutively larger as lowest rank of the network's grid-forming or grid-tied VSC is

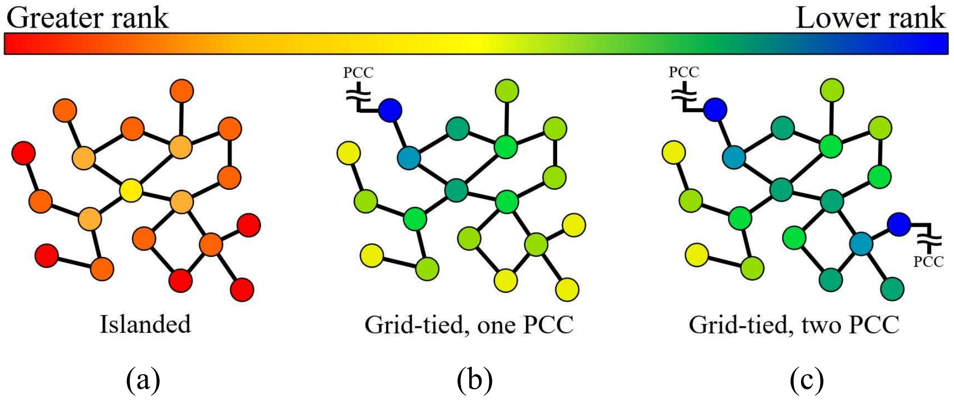

Fig. 3.2. Relative ranks of VSC nodes operating in different microgrid topologies. (a) Islanded microgrid. (b) Grid-tied at one PCC. (c) Grid-tied at two PCC.

propagated from one VSC to another. At most, the ranks of tied, neighboring VSCs differ by 1. This is illustrated with nodes in Fig. 3.2.

If the microgrid is divided into smaller networks or the present grid-forming, voltage-controlled source is disconnected, the next lowest-ranked VSC within the system immediately transitions to voltage-controlled operation. Furthermore, the direction of synchronization in the new network is immediately and automatically updated to point toward the new grid-forming VSC. If two islanded microgrids, each with their own independent grid-forming VSC, are tied together at a single line, the lowest-ranking grid-forming VSC is selected as the voltage-controlled VSC of the combined system. Then, the rank of this voltage-controlled VSC forces a shift of synchronization directionality within the secondary microgrid as all VSCs follow the new system's voltage-controlled, grid-forming VSC.

The adaptive ranking scheme solves both topology challenges described in Section I. Since the leading VSC is either tied directly to the utility grid or operating in voltage control mode, all synchronization within the network occurs in its direction. When the line between two VSCs is commanded to close, the VSC of greater rank, i.e. farther from the utility PCC or grid-forming VSC, performs the synchronization. The ranks of VSCs within a microgrid automatically adapt to any topology changes, ensuring seamless transitions between operational modes and system configurations. Similarly, a grid-forming VSC is no longer a vulnerability to the islanded microgrid as it is automatically replaced when/if it disconnects.

3.2 Ranking optimization

The presented ranking scheme ensures that internal synchronization within a mesh, islanded microgrid is performed by the VSC furthest from the grid-forming source, as defined by the number of VSCs between them. This strategy is supported by Fig. 3.3, which depicts the reactive power produced by 10 VSCs for two simulated controllers. This experiment studies the performance of an islanded microgrid whose topology forms an incomplete ring. VSC_1 operates in voltage control mode. At t = 0.3 seconds, the line between VSC_9 and VSC_{10} is commanded to close and synchronization begins. In a community microgrid where line inductance is minimal, the phase shift between VSC_9 and VSC_{10} is negligible and the line simply closes in, completing the ring. In this study, each line inductance is raised to 5mH and synchronization between VSC_9 and VSC_{10} is required.

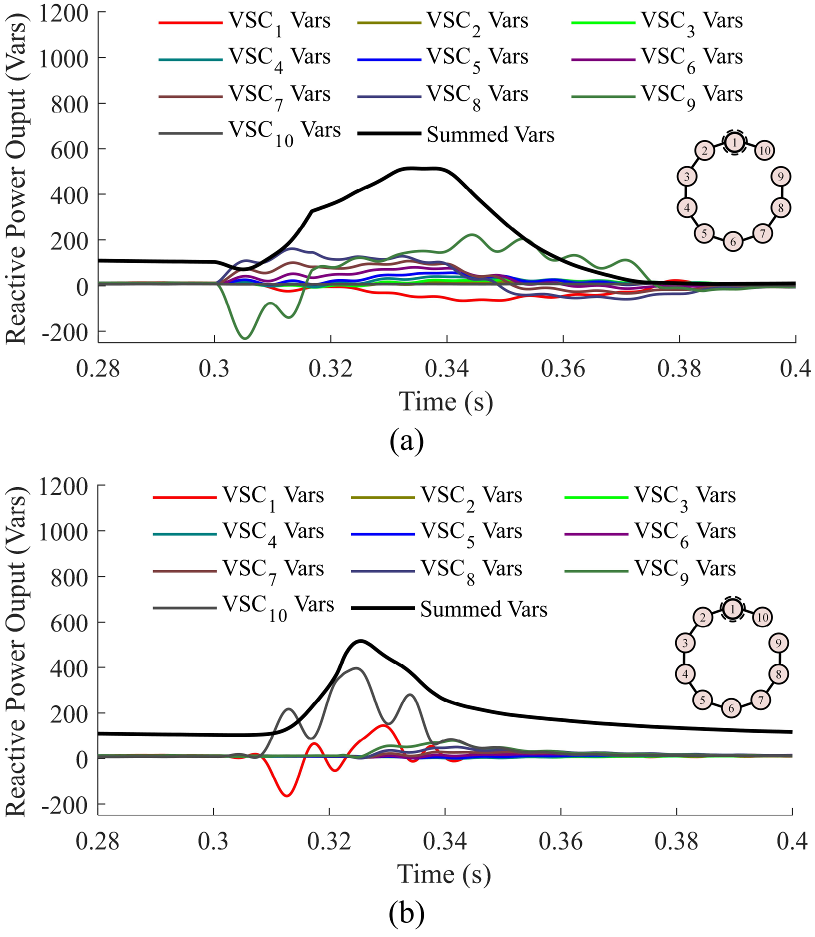

Fig. 3.3. Reactive power performance of VSCs operating under different control strategies during an internal synchronization event. Tie line between VSC_9 and VSC_{10} is commanded to close at t = 0.3 seconds. (a) Presented ranking scheme - VSC_9 synchronizes to VSC_{10}. (b) Reverse synchronization – VSC_{10} synchronizes to VSC_9.

Fig. 3.3a shows the reactive power output of each VSC, as well as their sum, for the ranking scheme defined by (3.2). Because VSC_9 is further from the grid-forming source, it transitions to voltage-control mode and performs synchronization. The phase shift induced by VSC_9 causes a cascade of reactive power generation from every current-controlled VSC between VSC_9 and VSC_1. The quantity of reactive power produced per VSC is dependent on its distance from VSC_1, where VSC_9 generates the most, followed by VSC_8 and VSC_7.

Fig. 3.3b shows the reactive power output of each VSC, as well as their sum, for a control scheme that requires the reverse synchronization strategy of (3.2). Here, VSC_{10} performs the synchronization to VSC_9. The total reactive power generated in the microgrid is approximately the same as in Fig. 3.3a, at just over 500 Vars. However, this power is being generated primarily by VSC_{10} rather than being distributed among all VSCs. Under extreme conditions with wide phase shifts within a mesh microgrid, the reactive power spike from a single VSC may damage converter hardware or trip the inverter, impacting the resiliency of the microgrid. For this reason, the presented ranking scheme is optimal for internal synchronizations.

3.3 Case studies and discussion

The following case studies offer a demonstration of the proposed adaptive rank-based MPC operating in various environments and topologies. First, a three-VSC microgrid cluster is presented to emphasize adaptive ranking functionality and its impact on major grid events, such as islanding and synchronization. Second, a brief comparison to traditional control structures is introduced by incorporating real-time simulations (RTS) of a ten-VSC microgrid undergoing synchronization. Finally, several more RTS studies are examined to verify the rank-based controller's performance in a dynamic microgrid with MPCC.

3.3.1 Three-VSC ranking analysis studies

The proposed controller and ranking scheme are implemented in MATLAB Simulink for system level simulations. Four case studies test the performance of the adaptive rank-based controller under four topology shifts in a microgrid network with three single-phase VSCs, as outlined in Fig. 3.4. The physical and electrical parameters of the simulated circuit are included in Table 3.1. N, the maximum theoretical number of VSCs within the system used to calculate initial ranks R_o, is set to 100.

Case 1 tests the performance of predictive VSCs with the proposed adaptive ranking scheme throughout a grid-tying transition. Fig. 3.5a shows the ranks of each VSC over time. Prior to t = 0.5 seconds, VSC_1 possesses the lowest rank (R_1=$R_{o,1}$=100) thus operates in voltage-control mode while VSC_2 and VSC_3 operate in current-control mode. At t = 0.5 seconds, VSC_3 is commanded to synchronize to the utility grid and its rank immediately adapts (R_3=1). VSC_3 transitions to voltage-control mode to perform the synchronization, and because of the shift in

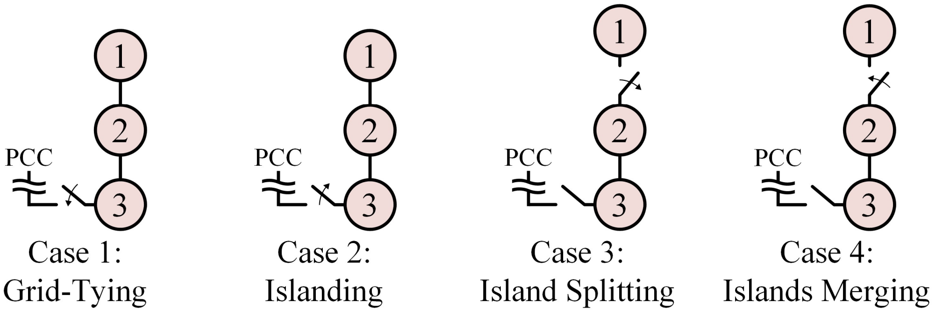

Case 1: Grid-Tying
Case 2: Islanding
Case 3: Island Splitting
Case 4: Islands Merging

Fig. 3.4. Three-VSC microgrid configurations.

Table 3.1. Three-VSC system specifications.

Parameter	Value
DC Link Voltages V_{DC}	200V
Sampling Time T_s	20µs
Filter Inductor L_f	3mH
Filter Resistance R_f	0.03Ω
Filter Capacitance C_f	10µF
Rated Grid Voltage V_G	$95V_{pk}$
Rated Island Voltage V_o	$100V_{pk}$

ranks, VSC$_1$ transitions to current-control mode. The seamless synchronization to the utility grid is completed at t = 0.65 seconds, as shown in Fig. 3.5b, when the line is closed in and VSC$_3$ returns to current-control mode. Active power remains stable throughout the transition, as is evident from Fig. 3.5c.

Case 2 explores the use of ranked predictive controllers during an islanding event. Fig. 3.6a shows the ranks of each VSC over time. While directly grid-tied, the rank of VSC$_3$ (R_3=1) ensures all VSCs operate in current control mode, as both VSC$_1$ and VSC$_2$ are tied to a lesser-

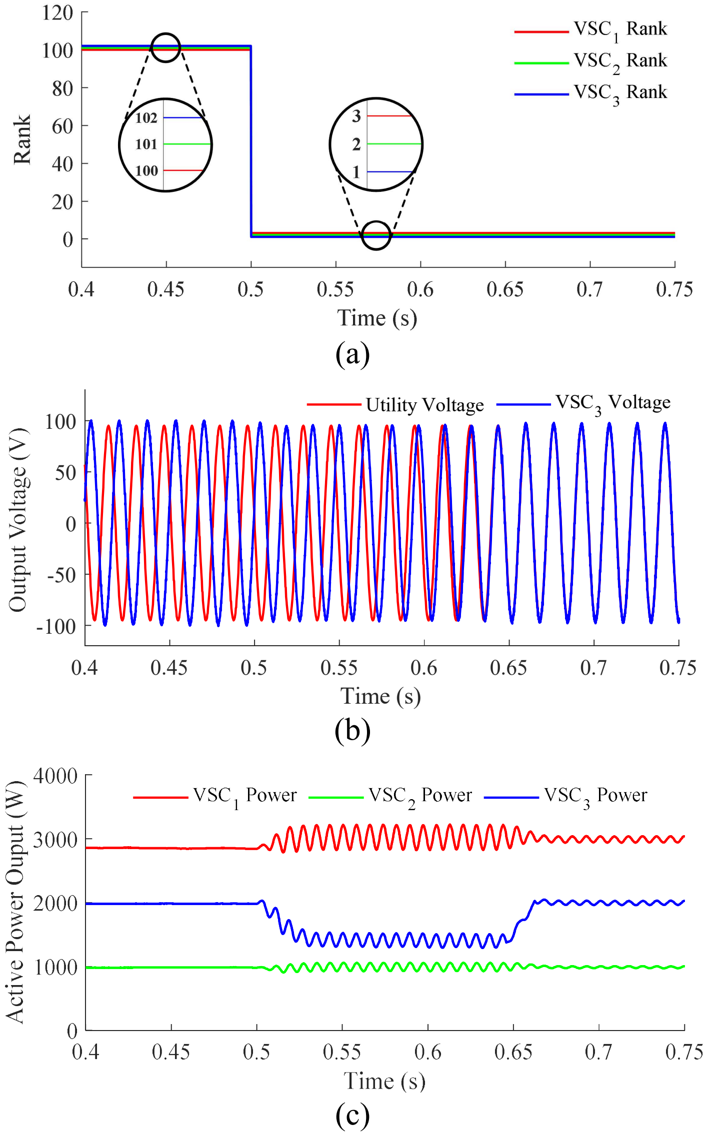

Fig. 3.5. Case 1 operation of rank-based VSCs during a grid-tie event at t = 0.5 seconds. (a) VSC$_1$, VSC$_2$, VSC$_3$ ranks. (b) Utility voltage, VSC$_3$ voltage, (c) VSC$_1$, VSC$_2$, VSC$_3$ active power.

ranked neighbor. VSC$_3$ islands from the utility grid at t = 0.5 seconds and VSC ranks increase accordingly. VSC$_1$'s rank (R_1=$R_{o,1}$=100) is now the lowest of the islanded network, causing VSC$_1$ to transition to voltage-control mode while VSC$_2$ and VSC$_3$ remain in current control mode. The slight shift in voltage magnitude and frequency shown in Fig. 3.6b is evidence of successful islanding from the utility grid. Active power throughout the transition is shown in Fig. 3.6c.

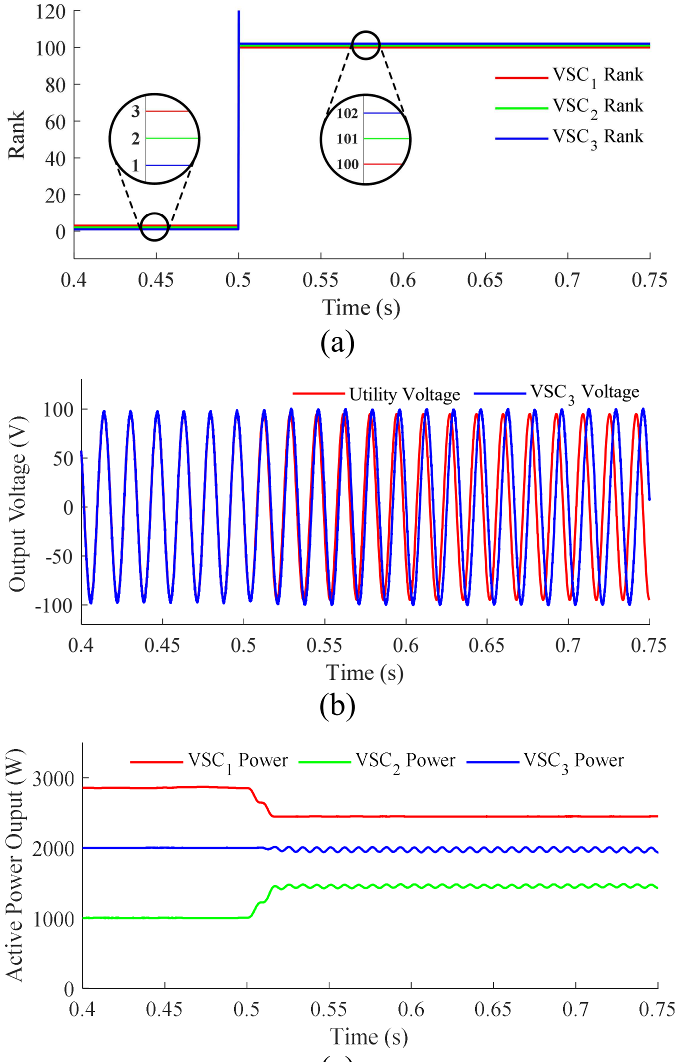

(a)

(b)

(c)

Fig. 3.6. Case 2 operation of rank-based VSCs during an islanding event at t = 0.5 seconds. (a) VSC$_1$, VSC$_2$, VSC$_3$ ranks. (b) Utility voltage, VSC$_3$ voltage, (c) VSC$_1$, VSC$_2$, VSC$_3$ active power.

Case 3 tests a dynamic topology that comprises an islanded microgrid split into two smaller grid clusters. Fig. 3.7a shows the ranks of each VSC over time. Prior to t = 0.5 seconds, VSC_1 possesses the lowest rank (R_1=$R_{o,1}$=100) and supports the islanded system in voltage-control. At t = 0.5 seconds, the tie line between VSC_1 and VSC_2 is opened. VSC_1 continues operating in voltage-control mode as its own, independent grid node. VSC_2 possesses the lowest rank (R_2=$R_{o,2}$=200) of the second grid cluster and transitions to voltage-control mode as well.

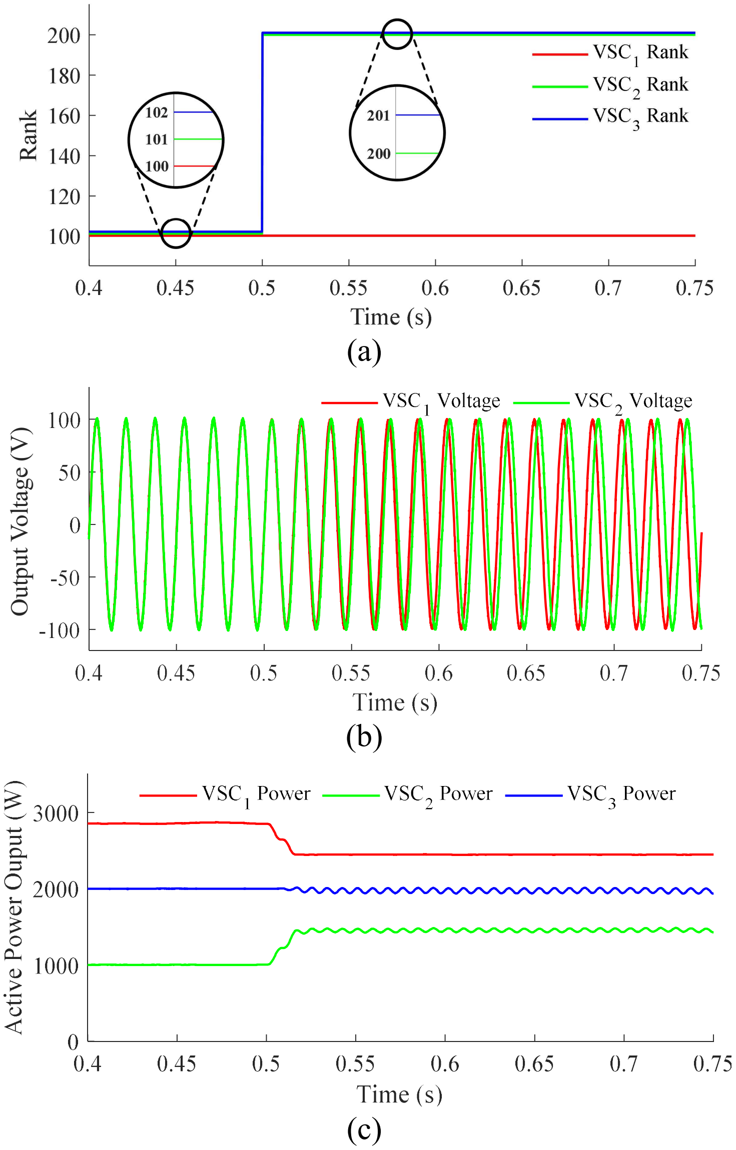

Fig. 3.7. Case 3 operation of rank-based VSCs during an island splitting event at t = 0.5 seconds. (a) VSC_1, VSC_2, VSC_3 ranks. (b) VSC_1 voltage, VSC_2 voltage, (c) VSC_1, VSC_2, VSC_3 active power.

VSC$_3$ remains in current-control mode throughout the transition. Fig. 3.7b shows the voltage waveforms of both isolated grid clusters. An artificial frequency deviation is added to the control loop of VSC$_2$ to better illustrate the separation. Active power throughout the transition is shown in Fig. 3.7c.

Case 4 tests the reverse of Case 3, with a dynamic topology that comprises two islanded grid clusters merging into a single, larger, islanded microgrid. Fig. 3.8a shows the ranks of each VSC over time. The first grid cluster contains just VSC$_1$ operating in voltage-control mode. The

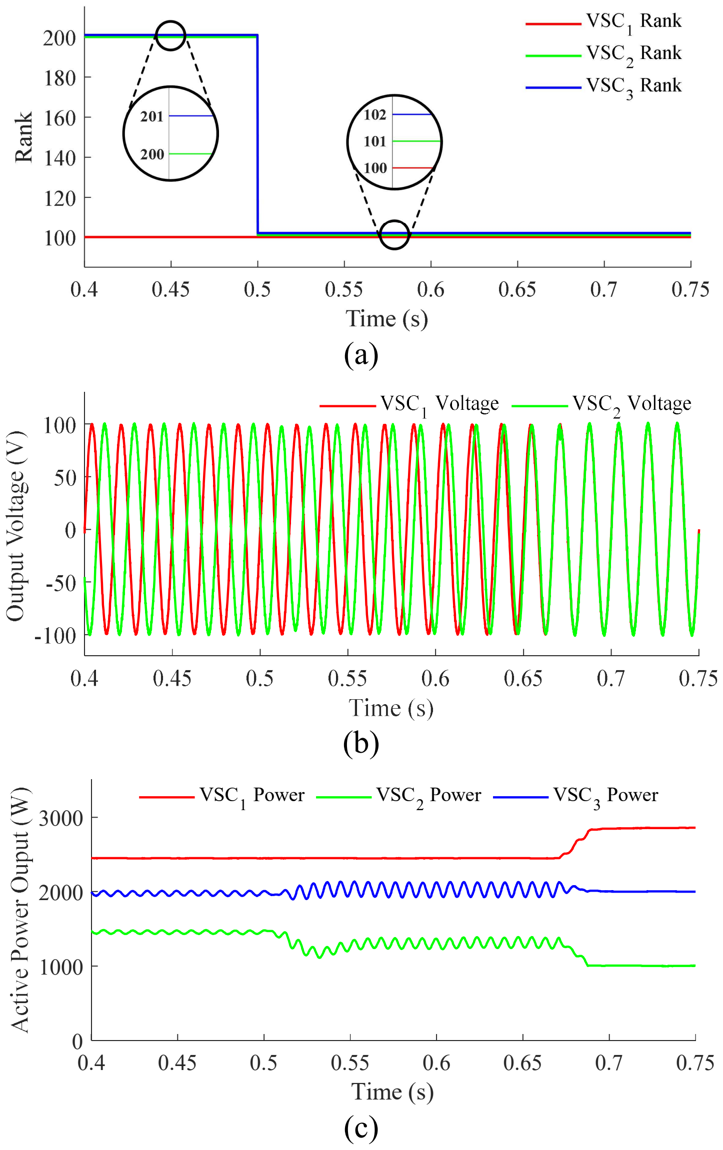

Fig. 3.8. Case 4 operation of rank-based VSCs during an islands merging event at t = 0.5 seconds. (a) VSC$_1$, VSC$_2$, VSC$_3$ ranks. (b) VSC$_1$ voltage, VSC$_2$ voltage, (c) VSC$_1$, VSC$_2$, VSC$_3$ active power.

second grid cluster comprises VSC_2 and VSC_3. The lower rank of VSC_2 ($R_2=R_{o,2}=200$ vs. $R_3=R_{o,3}=300$) causes it to operate in voltage-control mode while VSC_3 meets its power reference in current-control mode. The tie line between VSC_1 and VSC_2 is commanded to close at t = 0.5 seconds. VSC_2 immediately adapts to the lower rank of VSC_1 and begins synchronizing its waveform to that of VSC_1 while VSC_3 follows. Seamless synchronization between the grid clusters is achieved at t = 0.67 seconds, as is evident in Fig. 3.8b, when the line between VSC_1 and VSC_2 is closed in and VSC_2 transitions to current-control mode. VSC_1 continues operating in voltage-control mode as the grid-forming source of the merged microgrid with rank $R_1=100$. Active power throughout the transition is shown in Fig. 3.8c.

3.3.2 Ten-VSC controller comparison and additional studies

The proposed intelligent rank-based MPC is tested experimentally via the Opal-RT real time environment. Fig. 3.9 depicts the proposed topology for the following case studies. Ten

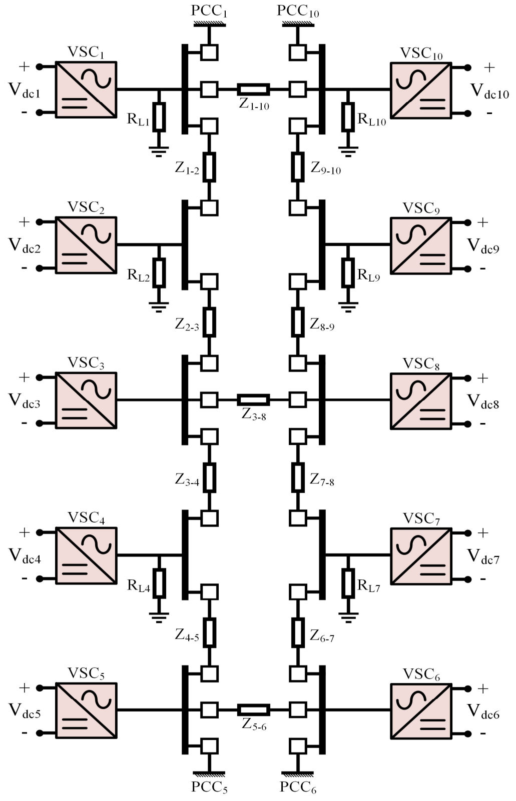

Fig. 3.9. Ten-VSC microgrid topology.

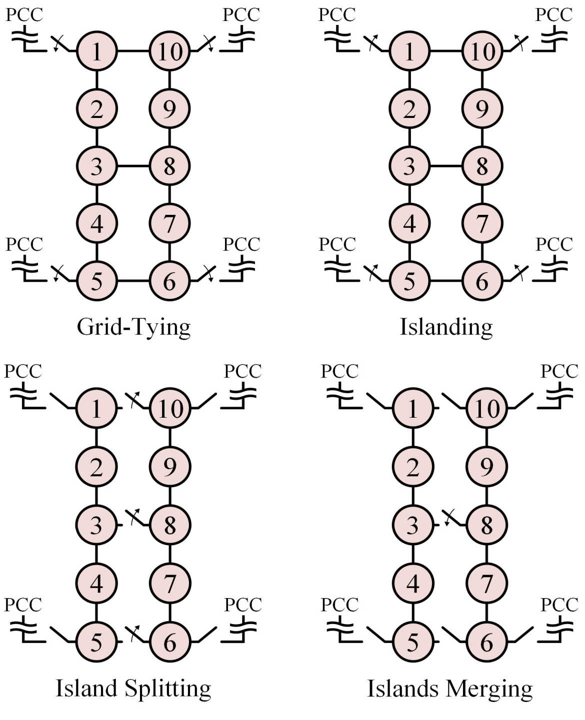

Fig. 3.10. Four case study microgrid configurations.

Table 3.3. Ten-VSC system specifications

Parameter	Value
DC Link Voltages V_{DC}	200V
Sampling Time T_s	20μs
Filter Inductor L_f	3mH
Filter Resistance R_f	0.03Ω
Filter Capacitance C_f	10μF
Rated Grid Voltage V_G	$90V_{pk}$
Rated Island Voltage V_o	$100V_{pk}$

Table 3.2. Grid-tying controller comparison metrics

Metric	Non-adaptive MPC	Non-adaptive Droop	Adaptive MPC
Synchronization time	N/A	N/A	112ms
VSC_6 peak voltage mag.	104.1V	105.6V	107.5V
VSC_6 min. voltage mag.	73.4V	78.4V	92.2V
VSC_6 peak active power	8490W	8750W	3160W
Comparative energy losses (first 0.2 seconds of sync.)	14.9J	809J	negligible

identical VSCs, each supplied with its own DC source, operate in a low voltage microgrid, where PCC_1, PCC_5, PCC_6, and PCC_{10} provide coupling points to the utility grid. Breakers at each local bus provide a means of reconfiguring the microgrid in real time. Parameters of the simulated circuit are included in Table 3.3 and individual configurations for the four presented case studies are shown in Fig. 3.10. The utility grid and islanded VSC rated voltage amplitudes differ to demonstrate magnitude synchronization as well as phase. For simplicity, integer IDs of the VSCs match the labels 1-10, and *N*, the maximum theoretical number of VSCs within the system, is set to 100.

Case 5 offers a comparison between grid-tying microgrids with and without the proposed adaptive ranking control scheme. The results of this comparison are summarized in Table 3.2. Case 5a tests the performance of simple MPC controlled VSCs operating in a microgrid without adaptive ranking throughout the grid-tying transition. VSC_1 is a fixed voltage-controlled source in the islanded microgrid and VSC₆ is commanded to synchronize to the utility grid at t = 1.283 seconds. VSC₆ has no way to communicate its new synchronizing status with its neighboring nodes as it transitions to voltage control mode to synchronize with the utility waveform. Fig. 3.11a shows the immediate distortion of the output voltage waveform as VSC₁ and VSC₆ operate in competing voltage-control modes. Interference between the two grid-forming sources results in a VSC₆ bus volage magnitude that fluctuates wildly between 73V and 104V. The active powers of VSC₁ and VSC₆ also destabilize, as shown in Fig. 3.11b, with VSC₆ injecting a maximum of 8.5kW that is consumed by VSC₁. These large circulating currents within the microgrid cluster produce energy losses in the resistive distribution lines. Compared to an

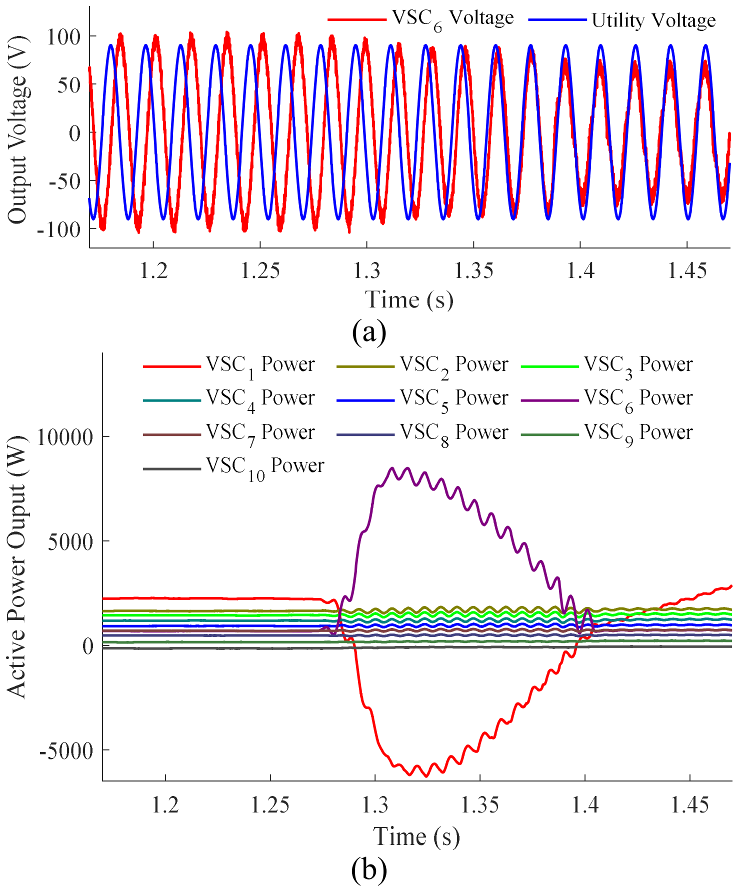

(a)

(b)

Fig. 3.11. Case 5a operation of non-adaptive MPC-equipped VSCs during a grid-tie event at t = 1.283 seconds. (a) VSC₆ voltage, utility voltage. (b) Ten VSC active power.

optimal, seamless transition, 14.9J of additional energy is lost within 0.2 seconds of synchronization beginning.

Case 5b tests the performance of droop controlled VSCs operating in the same grid-tying microgrid. Each droop controller couples active power with voltage magnitude and reactive power with phase angle. A deeper analysis of the droop controller is provided by [50]. VSC_6 is commanded to synchronize to the utility grid at t = 1.515 seconds, which it does by injecting proportional error terms into the voltage magnitude and phase control loops until the synchronizing waveforms match. Without adaptive droop gains within neighboring VSC controllers, VSC_6 struggles to synchronize the islanded microgrid to the utility waveform, as shown in Fig. 3.12a. Instead, microgrid bus voltage magnitude drops to 78V and destabilizes active power sharing among the parallel VSCs (Fig. 3.12b). The voltage discrepancy between the

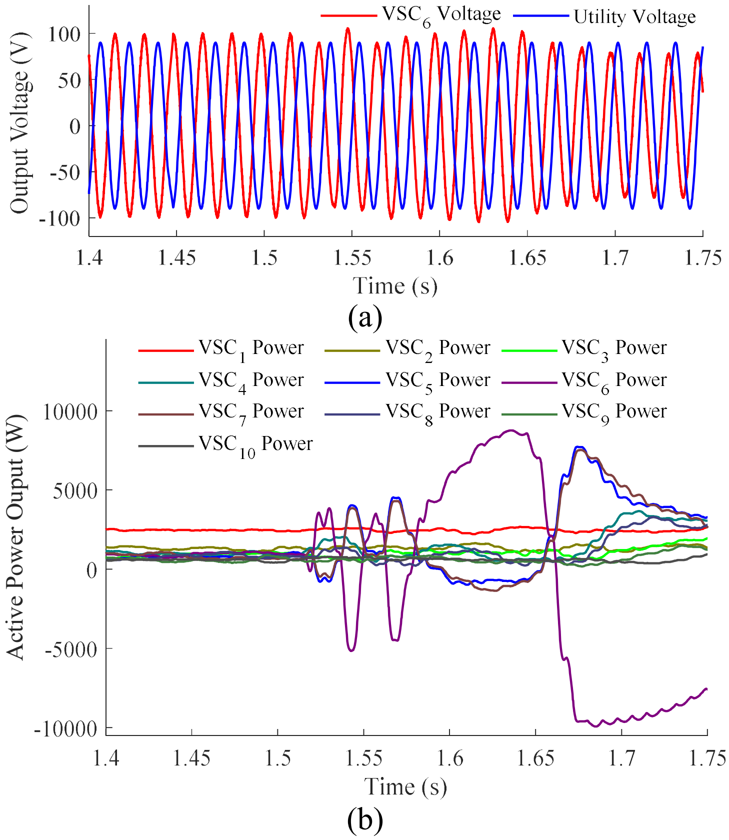

(a)

(b)

Fig. 3.12. Case 5b operation of non-adaptive droop-controlled VSCs during a grid-tie event at t = 1.515 seconds. (a) VSC_6 voltage, utility voltage. (b) Ten VSC active power.

islanded microgrid and VSC_6's target waveform produces active power spikes from VSC_6 of over 8.57kW before consuming nearly 10kW as power flow reverses around t = 1.65 seconds. These circulating currents, distributed between the parallel VSCs, generate energy loss in the distribution lines. Compared to an optimal, seamless transition, 809J of additional energy is lost within 0.2 seconds of synchronization beginning.

Case 5c tests the performance of predictive controlled VSCs with adaptive ranking throughout the grid-tying transition. VSC_1 bears the smallest rank (R_1=$R_{o,1}$=100) and operates as the islanded microgrid's voltage-controlled leader until VSC_6 is commanded to synchronize to the utility grid at t = 1.273 seconds. On command, R_6 immediately becomes 1 and VSC_6 begins operating in voltage-control mode as it synchronizes with the utility grid. The new, lower rank of VSC_6 is propagated through the network via the sparse communication layer, incremented at each node. VSC_1, no longer comprising the lowest local rank, transitions to current control mode. Unlike Case 5a, only one VSC operates in voltage control mode at any given time. When

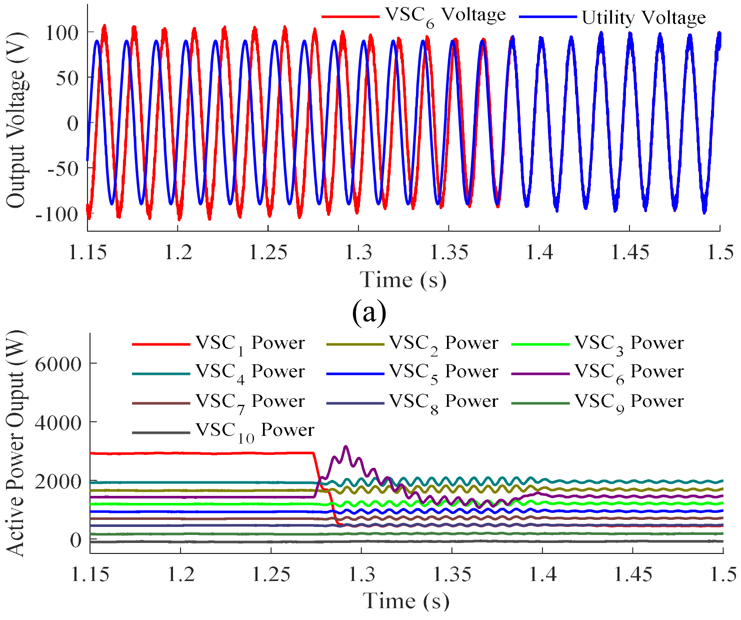

(a)

(b)

Fig. 3.13. Case 5c operation of rank-based predictive VSCs during a grid-tie event at t = 1.273 seconds. (a) VSC_6 voltage, utility voltage. (b) Ten VSC active power.

synchronization is completed at t = 1.385 seconds, PCC$_6$ is closed, VSC$_6$ returns to current control mode, and the other PCCs are free to close in to the utility grid. Fig. 3.13a depicts a successful synchronization to the utility grid while Fig. 3.13b shows the active power produced by each VSC throughout the transition. This study observes a higher peak voltage due to high-frequency filter noise but presents a solution for seamless synchronization without inefficient circulating currents.

Case 6 explores the use of ranked MPC controllers during an islanding event. At t = 0.956 seconds, all four PCCs disconnect from the utility grid, and VSC$_1$, possessing the lowest rank of the islanded microgrid (R_1=$R_{o,1}$=100), immediately and seamlessly transitions to voltage-control, grid-forming mode. All other VSCs observe lower ranks from connected neighbors, thus remain in current-control mode. Fig. 3.14a depicts the slow drift of voltage magnitude and phase from the utility waveform after isolation as VSC$_1$ generates a rigid sinusoid to support system voltage. Fig. 3.14b shows the active power outputs of all ten VSCs, including VSC$_1$, whose

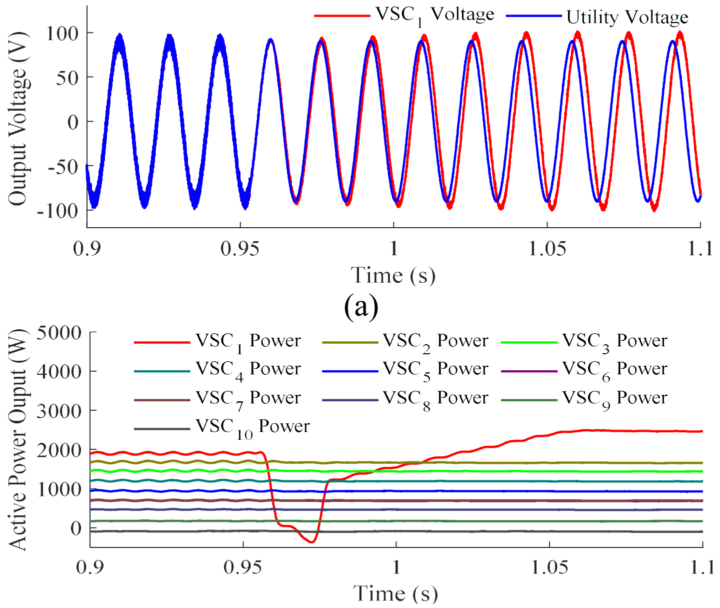

(a)

(b)

Fig. 3.14. Case 6 operation of rank-based predictive VSCs during an islanding event at t = 0.956. (a) VSC$_1$ voltage, utility voltage. (b) Ten VSC active power.

active power ramp is a result of the voltage amplitude change. VSCs 1-9 continue generating their respective active power references while VSC$_1$ compensates for the increased power consumption.

Case 7 tests a dynamic topology that comprises an islanded microgrid split into two smaller grid clusters. At t = 1.118 seconds, tie lines between VSC$_1$ and VSC$_{10}$, VSC$_3$ and VSC$_8$, and VSC$_5$ and VSC$_6$ are opened, isolating the left half of the islanded microgrid from the right. VSC$_1$ (R_1=$R_{o,1}$=100) continues to operate in voltage-control mode as the grid-forming leader of the left microgrid. On the right, VSC$_6$ possesses the lowest local rank (R_6=$R_{o,6}$=600) of its cluster and transitions to voltage-control mode as well. A small frequency deviation is introduced into the voltage reference of VSC$_6$ to better exhibit the isolation between the two islanded clusters, as shown in Fig. 3.15a. The change in VSC$_6$'s operational mode is evident in its active power shift in Fig. 3.15b. After splitting, the active power required from VSC$_1$ to support its bus voltage is reduced, while VSC$_6$ increases its generation to support the voltage of its own grid cluster.

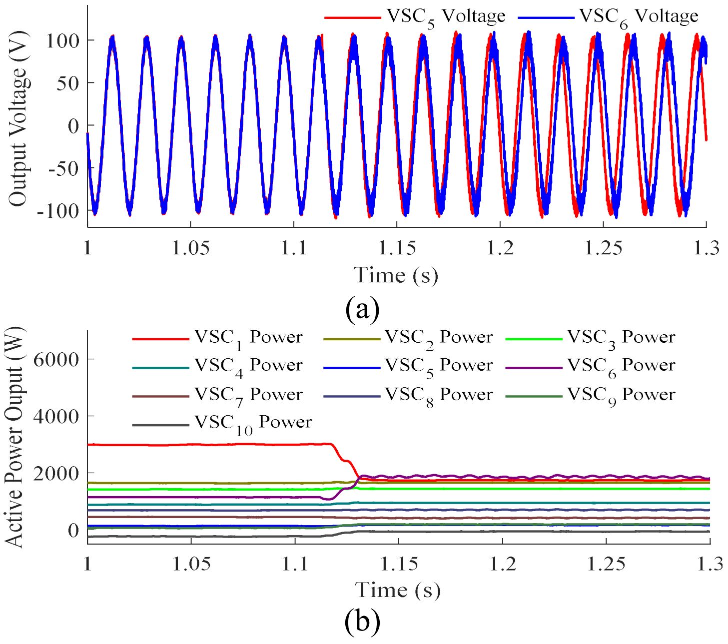

Fig. 3.15. Case 7 operation of rank-based predictive VSCs during an island splitting event at t = 1.118 seconds. (a) VSC$_5$ voltage, VSC$_6$ voltage. (b) Ten VSC active power.

Case 8 tests the reverse of Case 7, with a dynamic topology that comprises two islanded grid clusters merging into a single, larger, islanded microgrid. VSC$_1$ (R_1=100) operates in voltage-control mode in one grid cluster while VSC$_6$ (R_6=600) does so in the second cluster. At t = 1.561 seconds, the tie line between VSC$_3$ and VSC$_8$ is commanded to close, triggering a synchronization event between the two VSCs. VSC$_8$'s rank (R_8=602) is larger than VSC$_3$'s rank (R_3=102), thus VSC$_8$ adapts its rank to 103 and transitions to voltage-control mode for synchronization. The new, lower rank of VSC$_8$ (R_8=103) causes VSC$_6$ to adapt from voltage-control mode to current-control mode such that each grid cluster comprises one grid-forming source. Seamless synchronization of VSC$_8$ with VSC$_3$ is evident in Fig. 3.16a and completes at t = 1.631 seconds. VSC$_8$ returns to current-control mode and VSC$_1$ becomes the merged island's grid-forming source. Active powers throughout the transition are displayed in Fig. 3.16b, which clearly shows the excess active power generation administered by VSC$_6$ before synchronization, VSC$_6$ during synchronization, and VSC$_1$ after synchronization.

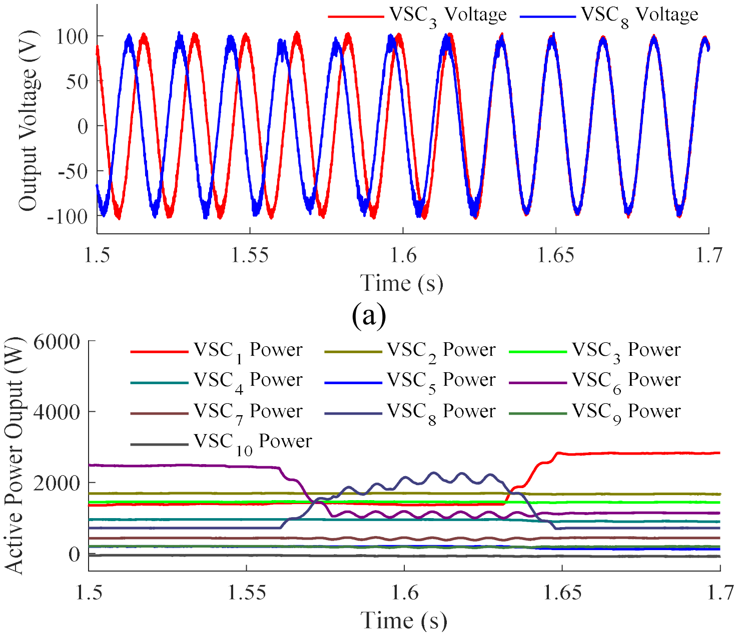

(a)

(b)

Fig. 3.16. Case 8 operation of rank-based predictive VSCs during an islands merging event at t = 1.561. (a) VSC$_3$ voltage, VSC$_8$ voltage. (b) Ten VSC active power.

The proposed rank-based predictive controller solves both dynamic microgrid topology limitations listed in the introduction. Ranks of priority VSCs, i.e. grid-forming or grid-tied, are assigned such that synchronization of grid-following, neighboring VSCs always occurs in their direction. Rank adaptability ensures correct operational behavior of every VSC in the system, regardless of network topology or utility coupling points. Relying on a voltage controlled VSC is no longer a vulnerability because any converter can be automatically called upon to take its place. The control scheme conducts synchronization and islanding in various topologies without sacrificing VSC performance, proving its effectiveness in a dynamic microgrid network with flexible boundaries.

Chapter 4 - Scalability Analysis

4.1 Expandability within a microgrid

A key characteristic of dynamic microgrids with flexible boundaries is the ability to resize the physical scope of clustered or islanded systems to meet performance objectives. Depending on loading, DER capacity, weather constraints, health of the distribution network, among other factors, optimal performance may mandate a single interconnected microgrid, several islanded clusters, or a topology that compromises between the two. This trait necessitates a widely expandable control scheme that operates reliably within both a tiny local VSC cluster and a large regional configuration. In the previous chapter, adaptive, rank-based MPC was demonstrated in a microgrid comprising three and ten VSCs. The controller must also be proven to function optimally in networks of hundreds or thousands of interconnected VSCs to verify resilient scalability.

The proposed ranking scheme and limited topology-mirroring communication structure are innately expandable to any scale. Distributed control enables near plug-and-play implementation where additional VSCs have no impact on the overall control framework within the microgrid. The simple rank-based controller presented in Chapter 3 ensures consistent behavior within a network of any size. However, communication with neighboring nodes is an important consideration when expanding the microgrid via additional DERs within the existing system boundaries. From (3.2), the controller is designed to observe the ranks of an arbitrary n number of neighbors, but these ranks must be provided via a physical communication architecture.

The assignment of initial rank R_o and integer ID is critical for the optimal performance of a regional and dynamic microgrid. From (3.1), constant N, the maximum theoretical number of distributed VSCs within the system, must be set sufficiently high to permit the future expansion of the microgrid network. Adequate selection of *N* ensures exactly one grid-forming VSC within an islanded cluster and compounds the importance of a VSC's unique ID. A VSC's integer ID is directly proportional to its initial rank, such that a low ID value results in a correspondingly sized initial rank. Because the VSC with minimal initial rank is selected for voltage-control within an islanded system, great care must be taken to assign and distribute the integer IDs among VSCs. In practice, VSCs with the greatest capacity for supporting grid voltage should be assigned the lowest IDs for superior islanded performance. Large battery banks are favorable as low-ID, grid-forming sources due to their scalable nature and ability to consume excess power in an islanded microgrid.

4.2 Communication infrastructure analysis

An overview of common wired communication architectures for the control of distributed VSCs is presented in the introduction. While wireless communication among distributed networks has been popularized in recent years, wired connections remain the industrial standard. Copper and fiber optic physical cabling are often employed for their speed and security advantages over wireless alternatives [78]. Here, an analytical evaluation is performed to compare the physical requirements of implementing each control scheme via wired infrastructure. The topology-mirroring, sparse communication layer matches the physical topology of the system, reducing additional hardware required to implement such a controller while enabling plug-and-play functionality. Each VSC controls the breakers on its own local bus that link to neighboring buses or the utility grid. Line closing commands are provided by a hypothetical centralized communication layer, but the controller could be adapted to generate commands locally to achieve system-wide performance objectives in future work. The benefits of a topology-mirroring layer are evident by comparing the necessary infrastructure of the typical communication schemes shown in Fig. 1.7. An analysis of the total distance of wired communication lines for centralized (D_c), multicentralized (D_m), and distributed topology-mirroring (D_t) schemes operating in a mesh microgrid (i.e. grid of microgrids) is presented below. A notable exclusion from this list is decentralized control, which benefits from a communication-less architecture but limits each VSC's awareness of the surrounding system, and thus adaptability. The following analysis makes several assumptions to simplify calculations. One general assumption is a circular microgrid topology such that one node may reside in the geographical center. Table 4.1 contains the values of variables used throughout the analysis.

Centralized communication incorporates a supervisory layer to control each VSC individually from a single control point. To simplify calculations, this control point is assumed to be at the center of the circular microgrid. The average distance between a given point within a circle and that circle's center, β_1, is given by

$$\beta_1 = \frac{2R_1}{3} \tag{4.1}$$

where R_1 is the radius of the microgrid. Deriving a realistic formulation for R_1 as a function of the total number of nodes in the system, N, is a considerable challenge. As N increases, the radius of the circular network will increase nonlinearly. Thus, an exponential variable γ is introduced to restrict estimated radius growth. The formulation for R_1 is given by

$$R_1 = d_n\left(N^{\gamma} - 1\right) \tag{4.2}$$

where d_n represents the real-world physical distance between neighboring (tied) VSCs and scales the radius proportionally. A fully centralized control scheme incorporates N connections to a centralized node, so the total distance of necessary communication infrastructure D_c becomes,

$$D_c = N\beta_1 \tag{4.3}$$

A multicentralized communication layer comprises small, localized node clusters operating in a centralized manner. A two-level multicentralized layer is considered for this analysis. The central nodes of each cluster, which are assumed to reside at the geographical center of the cluster, are further controlled by a secondary centralized layer. Since each local cluster can be considered its own circular microgrid with P nodes, the centralized formulation (4.1) can be used to calculate the average distance between any node in the cluster and that cluster's central node. The average radius of each cluster, R_2, is given by (4.4), and the total infrastructure distance of an average grid cluster, β_2, is given by (4.5).

$$R_2 = d_n\left(P^{\gamma} - 1\right) \tag{4.4}$$

$$\beta_2 = \left(P - 1\right)\frac{2R_2}{3} \tag{4.5}$$

There are N/P such clusters. The formulation for average distance between a given cluster central node and the center node of the secondary centralized control layer is identical to β_1 in (4.1). If each center node of the distributed local grid clusters comprises further data links to

Table 4.1. Communication analysis specifications

Variable	Value
Avg. distance between neighboring VSCs d_n	1
Exponential variable γ	0.5
Avg. number of VSCs in multicentralized cluster P	10
Avg. number of VSC neighbors C	2.5

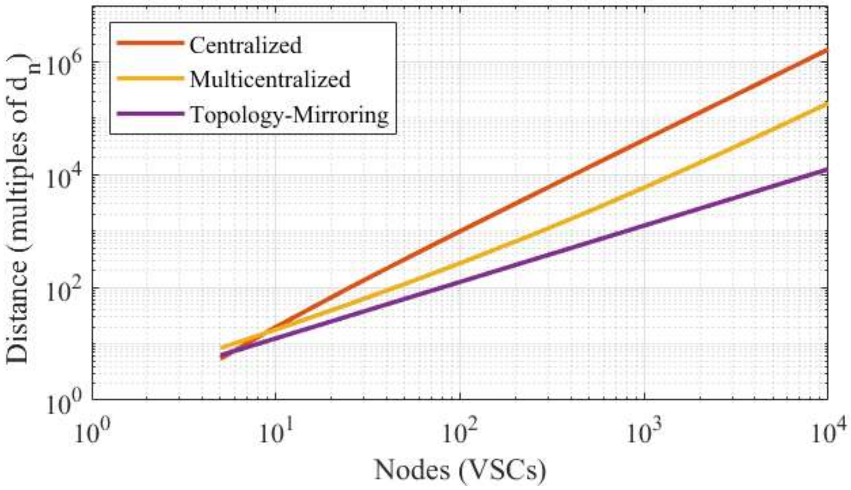

Fig. 4.1. Total distance of required wired communication infrastructure in a mesh microgrid.

other central nodes within the secondary control layer, then N/P such communication lines exist. The total infrastructure distance D_m is given by,

$$D_m = \frac{N}{P}\left(\beta_2 + \beta_1\right) \tag{4.6}$$

The formulation for total infrastructure distance of a topology-mirroring communication scheme D_t is comparatively simple, and given by (4.7), where C is the average number of connections to a given node in a fully interconnected mesh microgrid.

$$D_t = \frac{NC}{2} d_n \tag{4.7}$$

The physical infrastructure required for each communication scheme can be compared by evaluating (4.1)-(4.7) with the values in Table 4.1 and plotting the distances as a function of N. Fig. 4.1 shows the logarithmic growth of communication line distance as the total number of VSCs in the microgrid increases from 5 to 10,000. As expected, the centralized communication scheme requires the most infrastructure to function. Connections between each distributed node and a centralized controller present both implementation challenges due to distance and redundancy vulnerabilities. The studied multicentralized communication layer reduces the required infrastructure distance by an order of magnitude with a two-level design and ten VSCs per local cluster. Finally, the topology-mirroring scheme proposed in this paper requires the least wired infrastructure at a fraction of that needed for the next best scheme. With connections between only immediate neighbors, this sparse communication layer enables distributed control while maintaining flexibility and resiliency.

4.3 Challenges of expansion

The growth of distributed VSCs within a microgrid presents a voltage stability challenge for the proposed rank-based control scheme operating in islanded mode. Voltage support from a single grid-forming VSC is unlikely to offer sufficient performance if the network expands to a regional scale with thousands of nodes. A possible solution is to restrict the size and topology of the system to form localized clusters rather than a single mesh microgrid. In such a configuration, each cluster operates independently, but interconnection requires a supervisory control layer to enable synchronization between voltage-controlled sources. As the identity of the grid-forming source within an islanded cluster is adaptable, this necessitates extensive additional communication infrastructure and is an inadequate solution.

A similar implementation is achieved by reducing control variable N, the maximum number of nodes within a microgrid network. In (3.1), N also represents the minimum number of nodes within a series chain between grid-forming VSCs in an islanded system. While N is greater than the total VSC count, only one grid-forming source is possible. Reducing N enables multiple voltage-controlled sources, depending on islanded microgrid configuration, but reintroduces the challenge of synchronization between them. Without proper internal synchronization, currents circulating within the microgrid diminish stability and efficiency.

A better solution is the integration of the rank-based control scheme with a traditional, distributed droop control structure. The nature of droop control permits the use of multiple grid-forming sources for superior voltage support. Supplementing the classic droop structure with the proposed MPC ranking scheme as a secondary control layer enables the designation of several parallel voltage-controlled VSCs while offering adaptive, dual-mode operation. Implementation of such a controller combines the MPC of Chapter 2 with traditional Q-V and P-f droop curves for islanded voltage reference generation. All other signal references, including voltage synchronization references, remain the same. As previously stated, a reduction in ranking control variable N results in additional grid-forming sources being assigned throughout the mesh microgrid for superior voltage support and stability.

Chapter 5 - Conclusion and Future Research Roadmap

5.1 Summary

The major contribution of this thesis is the development of an adaptive rank-based MPC for dynamic microgrids with flexible boundaries. An analysis of typical VSC filter designs, as well as an evaluation of their respective discrete predictive models, is presented and evaluated on the merits of harmonic distortion, frequency response, and predictive operational modes. A finite-set model predictive controller offers a functional platform for verifying the functionality and performance of the proposed ranked control scheme throughout several experimental case studies. Experimental results demonstrate the deployment of such a control structure that enables the seamless transition between grid-connected and islanded modes by intelligently adapting individual VSC operating modes within a mesh microgrid. The controller is analyzed within dynamic network topologies featuring MPCC for increased robustness and resiliency. The ranking scheme is confirmed to improve the flexibility and performance of microgrids with flexible boundaries and internal synchronization.

Furthermore, the scalability of the proposed controller is investigated to verify correct functionality within vast, regional microgrid networks. Expansion is a critical issue facing distributed microgrid controllers as the penetration of DERs continues to rise. The advantages of the presented topology-mirroring distributed communication layer are supported analytically through the derivation of total communication infrastructure distance.

5.2 Future work

The dynamic nature of microgrid operation and control remains an ongoing field of research and development. The challenges outlined in this brief introductory chapter have no single solution and will continue to be considered as the energy sector slowly becomes more sustainable and reliable. Forecasted growth in renewable energy penetration makes grid stability a primary future concern and causes microgrids to become increasingly viable. Future research will continue to expand the resiliency of the power distribution system by means of advanced control techniques, cyber security, and topology elasticity.

Black start capability is an active area of research targeting grid reliability by reducing restoration times after an electrical blackout [19, 79]. In the context of microgrids, black start refers to the ability to reinitiate grid-tied operation from a deenergized network. Two main strategies for black start include single master operation, where a single VSC provides a voltage reference to the transitioning microgrid, and multiple master operation, where two or more VSCs support system voltage together. The optimal sequence of reenergization for a given topology is a complex problem that current literature explores, and factors such as critical loading, generation balancing, and full restoration time must be considered. The proposed synchronization at MPCC can be leveraged for black starts and sequential reenergization with further development.

An important step in the proliferation of DERs is the development of "plug and play" control techniques for integrating new generation sources. Complex communication schemes may assist in the control of power sharing and enable ancillary services to the microgrid but at the cost of restricted scalability. Decentralized and distributed control methods are popular due to their ease of use and installation. With additional research, the proposed topology-mirroring architecture will balance these factors to enable plug and play expansion while enabling other advanced capabilities [19].

Power system protection is a key field of ongoing research that is made significantly more complex by the addition of dynamic topologies. Active microgrid reconfigurations, such as those explored in this thesis, change potential system faults and optimal breaker set points. New protection schemes are being developed to adapt to changing topologies and bidirectional power flow without sacrificing reliability or performance [19].

As the costs of energy storage systems fall, electric battery installation is likely to become an attractive solution to intermittent, renewable generation challenges. The integration of such storage systems necessitates the development of strategic procedures for selecting type, capacity, location, and cost. Planning of these systems will consider an optimal balance of energy storage and renewable generation while considering the needs of critical and non-critical loads. Future research will build upon existing literature and explore various solutions for incorporating bulk energy storage on the power grid [19].

Cyber protection continues to be an important component of a 21st century smart grid. The power electronic interfaces used by DERs are susceptible to targeted attacks, and as the penetration of these systems increases, so too will the risks to the bulk power system. Further, advanced control architectures require a rising quantity of information and measurement data, making them more vulnerable to false data injections. Digital privacy is also a concern, both at the individual converter level and between regional grid clusters. A network of microgrids can span hundreds of miles and incorporate thousands of interconnected nodes, each with a cyber-physical security layer. Future research must balance the sharing of data for cooperation between microgrids with customer privacy and network security [19].

Like power system protection schemes, economic generation dispatch and load balancing are subject to the topology changes of a dynamic microgrid. Network reconfigurations may result in significant deviations to the expected resistive losses as current flows through different distribution lines in a sizable microgrid. This challenge is compounded by the inclusion of intermittent renewable power sources and energy storage devices at the grid edge. Further investigation of the proposed rank-based controller will attempt to optimize economic dispatch and power balancing within a microgrid of shifting topology, generation, and load [80, 81].

While this thesis focuses on an internally reconfigurable microgrid with clearly defined boundaries, future work may incorporate microgrids with dynamic boundaries to maximize resiliency. Existing literature explores the potential of such grid structures, where the shape and scale of a microgrid can adapt to supply critical loads or balance dispatch with distributed generation. These microgrids will seamlessly form, merge, grow, shrink, and disband as necessary, and are the culmination of MPCC topology where grid coupling junctions are ill-defined because the microgrid has no clear borders. These future networks will enable the intelligent control of distribution topology to achieve superior performance and resilient operation.

The presented rank-based controller for dynamic microgrid topologies will be further applied to power distribution systems of greater adaptability, scale, and DER penetration. Supervisory objective management will be developed to provide each VSC with distributed control of its surrounding network architecture, where data collection at the local AC bus and sparce communication framework enable a tertiary control layer to intelligently reconfigure the power system. In this way, a single controller will govern line opening and closing commands and enable adaptive VSC operational modes for optimal performance. Such distributed control benefits from rapid response time, resiliency, and eliminates the need for centralized management. In the future, artificial neural networks may be employed to determine real-time local microgrid topology for maintaining optimal power flow and power reserves while maximizing system efficiency. Further, weather forecasting will be applied to predict an appropriate network configuration from estimated PV and wind energy generation.

The ranked MPC will be expanded to comprise dozens of VSCs, loads, and utility coupling points within a microgrid. Adaptive ranking will be applied to droop control to enable multiple grid-forming sources for superior voltage support and stability within an islanded microgrid, as outlined in Chapter 4. MPC will remain the primary control loop of this architecture, but grid-forming VSCs will generate local voltage references from droop curves. Several studies are necessary to verify the functionality of the aforementioned controller amid dynamic microgrid topology comprising dozens or hundreds of nodes.

References

[1] C. ISO, "What the duck curve tells us about managing a green grid," *Calif. ISO, Shap. a Renewed Futur,* pp. 1-4, 2012.

[2] S. D'silva, M. Shadmand, S. Bayhan, and H. Abu-Rub, "Towards grid of microgrids: Seamless transition between grid-connected and islanded modes of operation," *IEEE Open Journal of the Industrial Electronics Society,* vol. 1, pp. 66-81, 2020.

[3] B. K. Bose, "Global energy scenario and impact of power electronics in 21st century," *IEEE Transactions on Industrial Electronics,* vol. 60, no. 7, pp. 2638-2651, 2012.

[4] Billion-Dollar Weather and Climate Disasters: Time Series [Online] Available: https://www.ncdc.noaa.gov/billions/time-series/US

[5] "Energy and Climate Change Research." United States Environmental Protection Agency. https://www.epa.gov/climate-research/energy-and-climate-change-research (accessed.

[6] F. Blaabjerg, D. M. Ionel, Y. Yang, and H. Wang, *Renewable energy systems technology overview and perspectives*. CRC Press LLC, 2017.

[7] K. Wang *et al.*, "A survey on energy internet: Architecture, approach, and emerging technologies," *IEEE Systems Journal,* vol. 12, no. 3, pp. 2403-2416, 2017.

[8] Z. Li, M. Shahidehpour, F. Aminifar, A. Alabdulwahab, and Y. Al-Turki, "Networked microgrids for enhancing the power system resilience," *Proceedings of the IEEE,* vol. 105, no. 7, pp. 1289-1310, 2017.

[9] Y. Wang, C. Chen, J. Wang, and R. Baldick, "Research on resilience of power systems under natural disasters—A review," *IEEE Transactions on Power Systems,* vol. 31, no. 2, pp. 1604-1613, 2015.

[10] F. Blaabjerg, Y. Yang, D. Yang, and X. Wang, "Distributed power-generation systems and protection," *Proceedings of the IEEE,* vol. 105, no. 7, pp. 1311-1331, 2017.

[11] M. Liserre, T. Sauter, and J. Y. Hung, "Future energy systems: Integrating renewable energy sources into the smart power grid through industrial electronics," *IEEE industrial electronics magazine,* vol. 4, no. 1, pp. 18-37, 2010.

[12] B. Kroposki *et al.*, "Achieving a 100% renewable grid: Operating electric power systems with extremely high levels of variable renewable energy," *IEEE Power and Energy Magazine,* vol. 15, no. 2, pp. 61-73, 2017.

[13] F. Blaabjerg and K. Ma, "Future on power electronics for wind turbine systems," *IEEE Journal of emerging and selected topics in power electronics,* vol. 1, no. 3, pp. 139-152, 2013.

[14] S. Kouro, J. I. Leon, D. Vinnikov, and L. G. Franquelo, "Grid-connected photovoltaic systems: An overview of recent research and emerging PV converter technology," *IEEE Industrial Electronics Magazine,* vol. 9, no. 1, pp. 47-61, 2015.

[15] J. DeVilbiss. Electricity Monthly Update [Online] Available: https://www.eia.gov/electricity/monthly/update/archive/february2021/

[16] M. H. Rehmani, M. Reisslein, A. Rachedi, M. Erol-Kantarci, and M. Radenkovic, "Integrating renewable energy resources into the smart grid: Recent developments in information and communication technologies," *IEEE Transactions on Industrial Informatics,* vol. 14, no. 7, pp. 2814-2825, 2018.

[17] A. Majzoobi and A. Khodaei, "Application of microgrids in supporting distribution grid flexibility," *IEEE Transactions on Power Systems,* vol. 32, no. 5, pp. 3660-3669, 2016.

[18] M. Agrawal and C. P. Agrawal, "Combating distance limitation for communications within Multiple Micro-Grids by Virtual routers," in *2016 International Conference on Electrical Power and Energy Systems (ICEPES)*, 2016: IEEE, pp. 571-576.

[19] M. N. Alam, S. Chakrabarti, and A. Ghosh, "Networked microgrids: State-of-the-art and future perspectives," *IEEE Transactions on Industrial Informatics,* vol. 15, no. 3, pp. 1238-1250, 2018.

[20] A. Khan, M. Hosseinzadehtaher, M. B. Shadmand, S. Bayhan, and H. Abu-Rub, "On the Stability of the Power Electronics-Dominated Grid: A New Energy Paradigm," *IEEE Industrial Electronics Magazine,* vol. 14, no. 4, pp. 65-78, 2020.

[21] V. Telukunta, J. Pradhan, A. Agrawal, M. Singh, and S. G. Srivani, "Protection challenges under bulk penetration of renewable energy resources in power systems: A review," *CSEE journal of power and energy systems,* vol. 3, no. 4, pp. 365-379, 2017.

[22] Q. Peng, Q. Jiang, Y. Yang, T. Liu, H. Wang, and F. Blaabjerg, "On the stability of power electronics-dominated systems: Challenges and potential solutions," *IEEE Transactions on Industry Applications,* vol. 55, no. 6, pp. 7657-7670, 2019.

[23] A. Y. Fard and M. B. Shadmand, "Multitimescale Three-Tiered Voltage Control Framework for Dispersed Smart Inverters at the Grid Edge," *IEEE Transactions on Industry Applications,* vol. 57, no. 1, pp. 824-834, 2020.

[24] J. P. Lopes, C. L. Moreira, and A. Madureira, "Defining control strategies for microgrids islanded operation," *IEEE Transactions on power systems,* vol. 21, no. 2, pp. 916-924, 2006.

[25] D. Pattabiraman, R. Lasseter, and T. Jahns, "Comparison of grid following and grid forming control for a high inverter penetration power system," in *2018 IEEE Power & Energy Society General Meeting (PESGM)*, 2018: IEEE, pp. 1-5.

[26] M. E. Elkhatib, W. Du, and R. H. Lasseter, "Evaluation of inverter-based grid frequency support using frequency-watt and grid-forming PV inverters," in *2018 IEEE Power & Energy Society General Meeting (PESGM)*, 2018: IEEE, pp. 1-5.

[27] W. Du, Q. Jiang, M. J. Erickson, and R. H. Lasseter, "Voltage-source control of PV inverter in a CERTS microgrid," *IEEE Transactions on Power Delivery,* vol. 29, no. 4, pp. 1726-1734, 2014.

[28] G. G. Talapur, H. M. Suryawanshi, L. Xu, and A. B. Shitole, "A reliable microgrid with seamless transition between grid connected and islanded mode for residential community with enhanced power quality," *IEEE Transactions on Industry Applications,* vol. 54, no. 5, pp. 5246-5255, 2018.

[29] C. Zheng, T. Dragičević, and F. Blaabjerg, "Current-sensorless finite-set model predictive control for LC-filtered voltage source inverters," *IEEE Transactions on Power Electronics,* vol. 35, no. 1, pp. 1086-1095, 2019.

[30] P. Cortés, M. P. Kazmierkowski, R. M. Kennel, D. E. Quevedo, and J. Rodríguez, "Predictive control in power electronics and drives," *IEEE Transactions on industrial electronics,* vol. 55, no. 12, pp. 4312-4324, 2008.

[31] F. Garcia-Torres, C. Bordons, and S. Vazquez, "Voltage predictive control for microgrids in islanded mode based on fourier transform," in *2015 IEEE International Conference on Industrial Technology (ICIT)*, 2015: IEEE, pp. 2358-2363.

[32] P. Zanchetta, M. Degano, J. Liu, and P. Mattavelli, "Iterative learning control with variable sampling frequency for current control of grid-connected converters in aircraft

power systems," *IEEE Transactions on Industry Applications,* vol. 49, no. 4, pp. 1548-1555, 2013.

[33] D. Zhang, "Operation of microgrid at constant frequency with a standby backup grid-forming generator," in *2016 IEEE International Conference on Power System Technology (POWERCON)*, 2016: IEEE, pp. 1-6.

[34] S. K. Jha and D. Kumar, "Robust Decentralized Control of Parallel type Autonomous Microgrid structure," in *2018 International Conference on Applied Electromagnetics, Signal Processing and Communication (AESPC)*, 2018, vol. 1: IEEE, pp. 1-6.

[35] A. Ipakchi and F. Albuyeh, "Grid of the future," *IEEE power and energy magazine,* vol. 7, no. 2, pp. 52-62, 2009.

[36] J. M. Guerrero, P. C. Loh, T.-L. Lee, and M. Chandorkar, "Advanced control architectures for intelligent microgrids—Part II: Power quality, energy storage, and AC/DC microgrids," *IEEE Transactions on industrial electronics,* vol. 60, no. 4, pp. 1263-1270, 2012.

[37] C. K. Sao and P. W. Lehn, "Control and power management of converter fed microgrids," *IEEE Transactions on Power Systems,* vol. 23, no. 3, pp. 1088-1098, 2008.

[38] D. T. Ton and M. A. Smith, "The US department of energy's microgrid initiative," *The Electricity Journal,* vol. 25, no. 8, pp. 84-94, 2012.

[39] J. M. Guerrero, M. Chandorkar, T.-L. Lee, and P. C. Loh, "Advanced control architectures for intelligent microgrids—Part I: Decentralized and hierarchical control," *IEEE Transactions on Industrial Electronics,* vol. 60, no. 4, pp. 1254-1262, 2012.

[40] M. Easley, S. Jain, M. Shadmand, and H. Abu-Rub, "Autonomous Model Predictive Controlled Smart Inverter with Proactive Grid Fault Ride-Through Capability," *IEEE Transactions on Energy Conversion,* vol. 35, no. 4, pp. 1825-1836, 2020.

[41] C.-C. Liu, "Distribution systems: reliable but not resilient?[In My View]," *IEEE Power and Energy Magazine,* vol. 13, no. 3, pp. 93-96, 2015.

[42] S. Parhizi, H. Lotfi, A. Khodaei, and S. Bahramirad, "State of the art in research on microgrids: A review," *Ieee Access,* vol. 3, pp. 890-925, 2015.

[43] S. Zhen, Y. Ma, F. Wang, and L. M. Tolbert, "Operation of a flexible dynamic boundary microgrid with multiple islands," in *2019 IEEE Applied Power Electronics Conference and Exposition (APEC)*, 2019: IEEE, pp. 548-554.

[44] M. S. Pilehvar, M. B. Shadmand, and B. Mirzfzal, "Analysis of Smart Loads in Nanogrids," *IEEE Access,* vol. 7, pp. 548-562, 2019, doi: 10.1109/ACCESS.2018.2885557.

[45] J. Wang, A. Pratt, and M. Baggu, "Integrated Synchronization Control of Grid-Forming Inverters for Smooth Microgrid Transition," in *2019 IEEE Power & Energy Society General Meeting (PESGM)*, 2019: IEEE, pp. 1-5.

[46] D. Ranamuka, A. P. Agalgaonkar, and K. M. Muttaqi, "Examining the interactions between DG units and voltage regulating devices for effective voltage control in distribution systems," *IEEE Transactions on Industry Applications,* vol. 53, no. 2, pp. 1485-1496, 2016.

[47] M. Hossain, J. Lu, M. Mahmud, and T. Aziz, "Advanced decentralized DER control for islanded microgrids," in *2014 Australasian Universities Power Engineering Conference (AUPEC)*, 2014: IEEE, pp. 1-5.

[48] Q.-C. Zhong, W.-L. Ming, and Y. Zeng, "Self-synchronized universal droop controller," *IEEE Access,* vol. 4, pp. 7145-7153, 2016.

[49] J. W. Simpson-Porco, Q. Shafiee, F. Dörfler, J. C. Vasquez, J. M. Guerrero, and F. Bullo, "Secondary frequency and voltage control of islanded microgrids via distributed averaging," *IEEE Transactions on Industrial Electronics,* vol. 62, no. 11, pp. 7025-7038, 2015.

[50] S. Shah, H. Sun, D. Nikovski, and J. Zhang, "Consensus-based synchronization of microgrids at multiple points of interconnection," in *2018 IEEE Power & Energy Society General Meeting (PESGM)*, 2018: IEEE, pp. 1-5.

[51] M. B. Shadmand, S. Jain, and R. S. Balog, "Autotuning technique for the cost function weight factors in model predictive control for power electronic interfaces," *IEEE Journal of Emerging and Selected Topics in Power Electronics,* vol. 7, no. 2, pp. 1408-1420, 2018.

[52] M. Easley, M. B. Shadmand, and H. Abu-Rub, "Hierarchical Model Predictive Control of Grid-Connected Cascaded Multilevel Inverter," *IEEE Journal of Emerging and Selected Topics in Power Electronics,* 2020.

[53] M. Hosseinzadehtaher, A. Khan, M. Easley, M. B. Shadmand, and P. Fajri, "Self-healing Predictive Control of Battery System in Naval Power System with Pulsed Power Loads," *IEEE Transactions on Energy Conversion,* 2020.

[54] M. B. Shadmand, M. Mosa, R. S. Balog, and H. Abu-Rub, "Model predictive control of a capacitorless matrix converter-based STATCOM," *IEEE Journal of Emerging and Selected Topics in Power Electronics,* vol. 5, no. 2, pp. 796-808, 2016.

[55] M. Easley, M. Shadmand, and H. A. Abu-Rub, "Computationally-efficient Optimal Control of Cascaded Multilevel Inverters with Power Balance for Energy Storage Systems," *IEEE Transactions on Industrial Electronics,* pp. 1-1, 2021, doi: 10.1109/TIE.2020.3048281.

[56] X. Li, H. Zhang, M. B. Shadmand, and R. S. Balog, "Model predictive control of a voltage-source inverter with seamless transition between islanded and grid-connected operations," *IEEE Transactions on Industrial Electronics,* vol. 64, no. 10, pp. 7906-7918, 2017.

[57] M. S. Khan and M. Iravani, "Supervisory hybrid control of a micro grid system," in *2007 IEEE Canada Electrical Power Conference*, 2007: IEEE, pp. 20-24.

[58] O. H. Abu-Rub, A. Y. Fard, M. F. Umar, M. Hosseinzadehtaher, and M. B. Shadmands, "Towards Intelligent Power Electronics-Dominated Grid via Machine Learning Techniques," *IEEE Power Electronics Magazine,* vol. 8, no. 1, pp. 28-38, 2021.

[59] F. R. Yu, P. Zhang, W. Xiao, and P. Choudhury, "Communication systems for grid integration of renewable energy resources," *IEEE network,* vol. 25, no. 5, pp. 22-29, 2011.

[60] A. Ahmad, M. H. Rehmani, H. Tembine, O. A. Mohammed, and A. Jamalipour, "IEEE Access Special Section Editorial: Optimization for emerging wireless networks: IoT, 5G, and smart grid communication networks," *IEEE Access,* vol. 5, pp. 2096-2100, 2017.

[61] B. Heile, "Smart grids for green communications [industry perspectives]," *IEEE Wireless Communications,* vol. 17, no. 3, pp. 4-6, 2010.

[62] X. Huang, K. Wang, J. Qiu, L. Hang, G. Li, and X. Wang, "Decentralized control of multi-parallel grid-forming DGs in islanded microgrids for enhanced transient performance," *IEEE Access,* vol. 7, pp. 17958-17968, 2019.

[63] A. Tavakoli, M. Negnevitsky, S. Lyden, and O. Haruni, "A decentralized control strategy for multiple distributed generation in islanded mode," in *2014 IEEE PES General Meeting| Conference & Exposition*, 2014: IEEE, pp. 1-5.

[64] E. Espina, J. Llanos, C. Burgos-Mellado, R. Cardenas-Dobson, M. Martinez-Gomez, and D. Saez, "Distributed Control Strategies for Microgrids: An Overview," *IEEE Access,* 2020.

[65] Q. Zhou, M. Shahidehpour, A. Paaso, S. Bahramirad, A. Alabdulwahab, and A. Abusorrah, "Distributed control and communication strategies in networked microgrids," *IEEE Communications Surveys & Tutorials,* vol. 22, no. 4, pp. 2586-2633, 2020.

[66] P. Wu, W. Huang, N. Tai, J. Xie, and B. Lv, "An advanced architecture of multiple microgrids interfacing with UCC," in *2017 IEEE Power & Energy Society General Meeting*, 2017: IEEE, pp. 1-5.

[67] M. Hossain, M. A. Mahmud, H. Pota, N. Mithulananthan, and R. Bansal, "Distributed control scheme to regulate power flow and minimize interactions in multiple microgrids," in *2014 IEEE PES General Meeting| Conference & Exposition*, 2014: IEEE, pp. 1-5.

[68] M. Moradzadeh, R. Boel, and L. Vandevelde, "Voltage coordination in multi-area power systems via distributed model predictive control," *IEEE Transactions on Power Systems,* vol. 28, no. 1, pp. 513-521, 2012.

[69] M. E. Nassar and M. M. Salama, "Adaptive self-adequate microgrids using dynamic boundaries," *IEEE Transactions on Smart Grid,* vol. 7, no. 1, pp. 105-113, 2015.

[70] R. Majumder and G. Bag, "Parallel operation of converter interfaced multiple microgrids," *International Journal of Electrical Power & Energy Systems,* vol. 55, pp. 486-496, 2014.

[71] B. Nun, M. F. Umar, and M. B. Shadmand, "Enabling Resilient Community Microgrids with Multiple Points of Common Coupling via a Rank-Based Model Predictive Control Framework," presented at the 2021 IEEE Applied Power Electronics Conference and Exposition (APEC), 2021.

[72] B. Nun, M. F. Umar, A. Karaki, and M. B. Shadmand, "Rank-Based Predictive Control Framework for Community Microgrids with Dynamic Reconfigurations and Multiple Points of Common Coupling," presented at the IEEE International Symposium on Power Electronics for Distributed Generation Systems (PEDG), 2021.

[73] I. S. Association, "519-2014-IEEE Recommended Practices and Requirements for Harmonic Control in Electric Power Systems," *New York, IEEE,* 2014.

[74] X. Chen, W. Wu, N. Gao, H. S.-H. Chung, M. Liserre, and F. Blaabjerg, "Finite control set model predictive control for LCL-filtered grid-tied inverter with minimum sensors," *IEEE Transactions on Industrial Electronics,* vol. 67, no. 12, pp. 9980-9990, 2020.

[75] H. A. Young, V. A. Marin, C. Pesce, and J. Rodriguez, "Simple finite-control-set model predictive control of grid-forming inverters with LCL filters," *IEEE Access,* vol. 8, pp. 81246-81256, 2020.

[76] N. Panten, N. Hoffmann, and F. W. Fuchs, "Finite control set model predictive current control for grid-connected voltage-source converters with LCL filters: A study based on different state feedbacks," *IEEE Transactions on Power Electronics,* vol. 31, no. 7, pp. 5189-5200, 2015.

[77] J. Benzaquen, A. Adib, F. Fateh, and B. Mirafzal, "A model predictive control scheme formulation for active rectifiers with LCL filter," in *2019 IEEE Energy Conversion Congress and Exposition (ECCE)*, 2019: IEEE, pp. 3758-3763.

[78] I. Serban, S. Céspedes, C. Marinescu, C. A. Azurdia-Meza, J. S. Gómez, and D. S. Hueichapan, "Communication requirements in microgrids: A practical survey," *IEEE Access,* vol. 8, pp. 47694-47712, 2020.

[79] C. Moreira, F. Resende, and J. P. Lopes, "Using low voltage microgrids for service restoration," *IEEE Transactions on Power Systems,* vol. 22, no. 1, pp. 395-403, 2007.

[80] Y. Ma *et al.*, "Real-time control and operation for a flexible microgrid with dynamic boundary," in *2018 IEEE Energy Conversion Congress and Exposition (ECCE)*, 2018: IEEE, pp. 5158-5163.

[81] Y. Du, X. Lu, J. Wang, and S. Lukic, "Distributed secondary control strategy for microgrid operation with dynamic boundaries," *IEEE Transactions on Smart Grid,* vol. 10, no. 5, pp. 5269-5282, 2018.

Appendix A - MATLAB script: MPC and cost function realization

```
function [S1, S2, S3, S4, Err_1, Err_2, Err_3] = fcn(Iref, Vdc, Ts, C, L, Vref, Vo, IL, Io,
Lambda_I)

S1 = 0;
S2 = 0;
S3 = 0;
S4 = 0;
ErrI = 0;
ErrV = 0;
Err_1 = 0;
Err_2 = 0;
Err_3 = 0;

% Initialize LC state space model
R = 10*L;
A= [-R/L -1/L; 1/C 0];
B= [1/L 0; 0 -1/C];
I= [1 0; 0 1];
Ad= expm(A.*Ts);
Bd = inv(A)*(Ad - I)*B;

if Lambda_I > 0      % pick I-vontrol or V-control
    Lambda_V = 0;
else
    Lambda_V = 1;
end


% Vinv = -Vdc
Vinv = -Vdc;
x= Ad*[IL;Vo] + Bd*[Vinv;Io];                          % solve discrete state space model
I_plus_one = x(1);
V_plus_one = x(2);
I_out_plus_one = I_plus_one - C*(V_plus_one-Vo)/Ts; % derive i_out from predicted values
ErrI = abs(Iref - I_out_plus_one);                     % current error
ErrV = abs(Vref - V_plus_one);                         % voltage error
Err_1 = Lambda_I*ErrI + Lambda_V*ErrV;                 % total error

% Vinv = 0
Vinv = 0;
x= Ad*[IL;Vo] + Bd*[Vinv;Io];
I_plus_one = x(1);
V_plus_one = x(2);
I_out_plus_one = I_plus_one - C*(V_plus_one-Vo)/Ts;
ErrI = abs(Iref - I_out_plus_one);
ErrV = abs(Vref - V_plus_one);
Err_2 = Lambda_I*ErrI + Lambda_V*ErrV;

% Vinv = Vdc
Vinv = Vdc;
x= Ad*[IL;Vo] + Bd*[Vinv;Io];
I_plus_one = x(1);
V_plus_one = x(2);
I_out_plus_one = I_plus_one - C*(V_plus_one-Vo)/Ts;
ErrI = abs(Iref - I_out_plus_one);
ErrV = abs(Vref - V_plus_one);
Err_3 = Lambda_I*ErrI + Lambda_V*ErrV;

% Choose minimum error
if Err_1 <= Err_2 && Err_1 <= Err_3
    S1 = 0;
    S2 = 1;
    S3 = 1;
    S4 = 0;
end
if Err_2 <= Err_1 && Err_2 <= Err_3 && Err_1 <= Err_3
    S1 = 0;
```

```
    S2 = 0;
    S3 = 1;
    S4 = 0;
end
if Err_2 <= Err_1 && Err_2 <= Err_3 && Err_3 <= Err_1
    S1 = 0;
    S2 = 0;
    S3 = 0;
    S4 = 1;
end
if Err_3 <= Err_1 && Err_3 <= Err_2
    S1 = 1;
    S2 = 0;
    S3 = 0;
    S4 = 1;
end
```

Appendix B - MATLAB script: ranking controller

```
function [Line, Grid, Freq_Adj, Ref_Mode, Ref_Mag, Rank_out, Lambda_I]  = fcn(Last_Line,
Last_Grid, Rank_in, Last_Mode, Last_Rank, Island, Connect, Error)

    num = length(Connect);  % total number of neighbors
    Freq_Adj = 0;
    Line = zeros(num,1);
    for i=1:1:num
        Line(i) = Last_Line(i);
    end

    ID = 1;                 % UNIQUE ID
    N = 100;                % total max number of VSCs within system
    Nat_rank = N*ID;        % Ro
    Rank_out = Nat_rank;    % initialize starting rank
    Ref_Mode = Last_Mode;   % initialize reference mode
    Ref_Mag = 1;            % initialize magnitude reference
    Lambda_I = 0;           % initialize weight factor

    Mult_error = zeros(num,1);
    Mult_slave = zeros(num,1);
    for i=1:1:num           % find min-ranked neighbor and their rank
        Mult_error(i) = Connect(i)*Error(i+1);
        Mult_slave(i) = Connect(i)*Rank_in(i);
        if Mult_slave(i) == 0
            Mult_slave(i) = 9999;
        end
    end
    [M,Slave_to] = min(Mult_slave);

    if Island > 0               % grid-tied command
        Rank_out = 1;           % always 1 for grid-tied
        Ref_Mag = 2;
        if Last_Grid == 0       % not connected yet
            Grid = 0;

            if (M<100) && (Last_Mode ~= 1)
                % If we're already syncing to a grid-tied neighbor then
                % we should wait for it to finish.
                Ref_Mode = Slave_to + 2;   % Map all ref_modes to the neighbor's index+2
                Rank_out = M + 1;          % output rank = min neighbor rank+1
                if Rank_out - Last_Rank(1) == 2
                    Rank_out = M + 0.1*N;
                end
                if Rank_out - Last_Rank(2) == 2
                    Rank_out = Last_Rank(1) + 0.2*N;
                end
                Rank_out = min(Nat_rank,Rank_out);
                if Error(1) < 25            % If it's this close, just close in to grid
                    Grid = 1;
                    Ref_Mode = 2;
                end
            else                            % Not connected AND neighbors aren't grid-tied
                                            % Control freq adjustment for sync to grid

                Ref_Mode = 1;
                if max(Mult_error) < 15
                    Freq_Adj = 1;
                else
                    Freq_Adj = 0;           % don't sync to grid if neighbor connection is bad
                end
                if Error(1) < 10            % finally synced to grid
                    Grid = 1;
                    Ref_Mode = 2;
                end
            end

        else % connected to grid
            Grid = 1;
```

```
        Ref_Mode = 2;
        Lambda_I = 1;
        for i=1:1:num
            if Connect(i) > 0
                Line(i) = 1;
            else
                Line(i) = 0;
            end
        end
    end

else  % islanded
    Grid = 0;

    % When connected to neighbors, sync to lowest rank and close in others
    if M < Nat_rank                     % a neighbor has a lower rank
        for i=1:1:num
            if Connect(i) > 0 && i~=Slave_to
                Line(i) = 1;            % close in other neighbors
            end
            if Connect(i) == 0
                Line(i) = 0;
            end
        end
        Rank_out = M + 1;
        if Rank_out - Last_Rank(1) == 2
            Rank_out = M + 0.1*N;
        end
        if Rank_out - Last_Rank(2) == 2
            Rank_out = Last_Rank(1) + 0.2*N;
        end
        Rank_out = min(Nat_rank,Rank_out);
        Ref_Mag = Slave_to + 2;
        if Last_Line(Slave_to) == 0
            if Error(Slave_to+1) < 10
                Line(Slave_to) = 1;
                Ref_Mode = Slave_to + 2;
            else
                Line(Slave_to) = 0;
                Ref_Mode = 1;
                Freq_Adj = 1;
            end
        else
            Line(Slave_to) = 1;
            Ref_Mode = Slave_to + 2;
            Lambda_I = 1;
        end
    else                                % we are lowest rank
        Ref_Mode = 1;
        for i=1:1:num
            if Connect(i) > 0
                Line(i) = 1;        % close in all connected neighbors
            else
                Line(i) = 0;
            end
        end
    end
end
```